Journal of the Geological Society

Quantifying rates of detachment faulting and erosion in the central Menderes Massif (western Turkey) by thermochronology and cosmogenic 10Be

J. T. Buscher, A. Hampel, R. Hetzel, I. Dunkl, C. Glotzbach, A. Struffert, C. Akal and M. Rätz

Journal of the Geological Society 2013, v.170; p669-683.
doi: 10.1144/jgs2012-132

Notes

Journal of the Geological Society, London, Vol. **170**, 2013, pp. 669–683. doi: 10.1144/jgs2012-132
Published *Online First* on June, 20, 2013

Quantifying rates of detachment faulting and erosion in the central Menderes Massif (western Turkey) by thermochronology and cosmogenic ^{10}Be

J. T. BUSCHER[1,2], A. HAMPEL[1*], R. HETZEL[3], I. DUNKL[4], C. GLOTZBACH[1]
A. STRUFFERT[3,5], C. AKAL[6] & M. RÄTZ[1,7]

[1]*Institut für Geologie, Leibniz Universität Hannover, Callinstraße 30, 30167 Hannover, Germany*
[2]*Present address: Dipartimento di Scienze della Terra, Università di Napoli 'Federico II', Largo San Marcellino 10, 80138 Napoli, Italy*
[3]*Institut für Geologie und Paläontologie, Westfälische Wilhelms-Universität Münster, Corrensstraße 24, 48149 Münster, Germany*
[4]*Geowissenschaftliches Zentrum der Universität Göttingen, Abteilung Sedimentologie/Umweltgeologie, Goldschmidtstraße 3, 37077 Göttingen, Germany*
[5]*Present address: Spilbrinkstraße 25, 59227 Ahlen, Germany*
[6]*Dokuz Eylül University, Engineering Faculty, Department of Geological Engineering, Tınaztepe Campus, Buca, 35160 Izmir, Turkey*
[7]*Present address: A.-Stifter-Str. 33, 38239 Salzgitter, Germany*
**Corresponding author (e-mail: hampel@geowi.uni-hannover.de)*

Abstract: Exhumation of rocks in extensional tectonic settings results from a combination of normal faulting and erosion but the relative contribution of these processes has rarely been quantified. Here we present new low-temperature thermochronological data and the first ^{10}Be-based catchment-wide erosion rates from the Boz Dağ region in the central Menderes Massif, which has experienced NNE–SSW extension since the Miocene. The slip rate of the shallow-dipping Gediz detachment fault, which defines the northern flank of the Boz Dağ block, is 4.3 (+3.0/−1.2) mm a^{-1}, as constrained by zircon (U–Th)/He ages of *c.* 4–2 Ma in the footwall. Apatite and zircon (U–Th)/He and fission-track ages from the northern flank of the Boz Dağ block yield exhumation rates of 0.6–2 km Ma^{-1} beneath the Gediz detachment, whereas those on the southern flank are only 0.2–0.6 km Ma^{-1}. Erosion of catchments on the northern and southern flanks proceeds at rates of 80–180 and 330–460 mm ka^{-1}, respectively. This marked contrast is a combined effect of the topographic asymmetry of the Boz Dağ block and differences in rock erodibility. If these erosion rates persisted in the past, rock exhumation on the northern flank occurred predominantly by tectonic denudation, whereas rocks on the southern flank were mainly exhumed by erosion.

Late-orogenic extension is a common phenomenon in orogenic belts (e.g. Dewey 1988) and typically results in the exhumation of rocks from mid-crustal levels along extensional shear zones and detachment faults (e.g. Lister & Davis 1989). Examples of regions undergoing active extension include the Basin-and-Range Province (e.g. Wernicke *et al.* 1988; Lister & Davis 1989), the European Alps (Ratschbacher *et al.* 1989; Mancktelow 1992; Fügenschuh *et al.* 1997; Frisch *et al.* 2000) and the Aegean region (Lee & Lister 1992; Bozkurt & Park 1994; Gautier & Brun 1994; Jackson 1994; Ring *et al.* 1999; Brichau *et al.* 2006; Grasemann *et al.* 2012). During the evolution of extensional ductile shear zones and brittle detachments, non- or weakly metamorphosed rocks are typically emplaced onto highly deformed metamorphic rocks, and older mylonitic fabrics are overprinted by younger cataclastic fault zones and discrete brittle faults (e.g. Crittenden *et al.* 1980; Lister & Davis 1989). An important aspect of extensional processes in orogenic belts is the fact that they provide a feasible mechanism for the relatively rapid exhumation of mid-crustal rocks (e.g. Ring *et al.* 1999).

The cooling history of rocks exhumed from mid-crustal levels to the Earth's surface is commonly inferred from low-temperature thermochronological methods, which allow reconstructions of time–temperature paths during exhumation (e.g. Fitzgerald *et al.* 1991; Gallagher *et al.* 1998; Reiners & Ehlers 2005). By estimating palaeo-geothermal gradients from a combination of geological, structural, and thermochronological data (e.g. Stockli 2005), rates of exhumation can be quantified. When interpreting exhumation rates derived from low-temperature thermochronology, it is necessary to take into account that exhumation is the sum of two major processes, tectonic denudation and erosion (e.g. England & Molnar 1990; Ring *et al.* 1999). The relative importance of both processes in regions of extension is commonly considered to be different for low-angle and high-angle normal faults. Investigations of metamorphic core complexes in the Basin-and-Range Province (e.g. Foster & John 1999; Brady 2002) and the Aegean region (John & Howard 1995; Brichau *et al.* 2008) revealed rapid cooling of metamorphic rocks within a few million years, from which high slip rates (*c.* 5–10 mm a^{-1}) on detachment faults were inferred. This implies that erosion should play only a minor role in the exhumation of rocks although remnants of supradetachment sedimentary basins that originally formed in the fault hanging walls indicate that erosion also contributed to the exhumation of metamorphic rocks. In contrast, exhumation rates in mountain ranges bounded by high-angle normal faults are usually lower (<2 mm a^{-1}; e.g. Stockli *et al.* 2002; Armstrong *et al.* 2003). These lower rates may be caused by lower slip rates on steeper faults and imply that erosion may be more important for the exhumation of such mountain ranges.

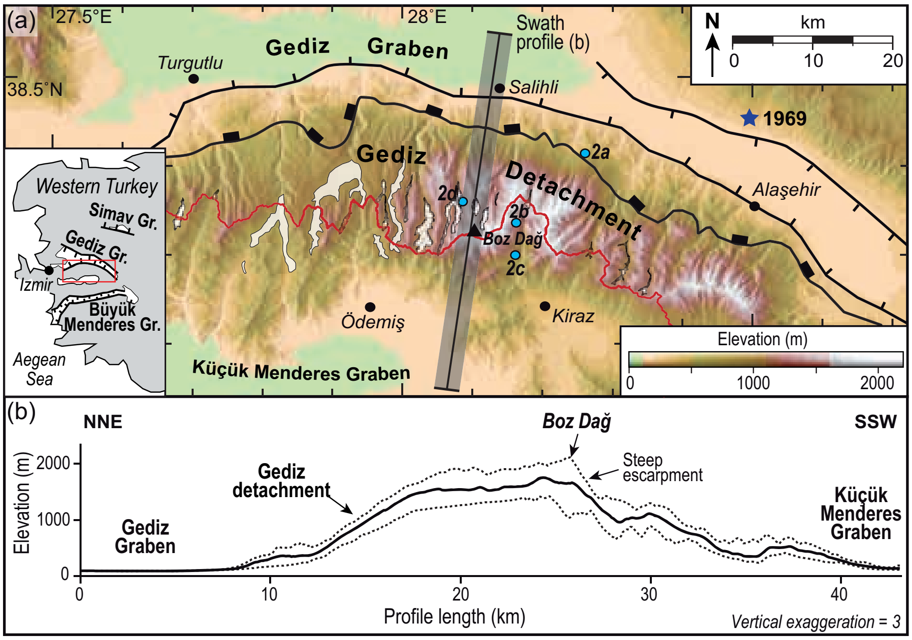

Fig. 1. (**a**) Topographic shaded relief map (90 m SRTM data) of the northern part of the central Menderes Massif, with the highest peak (Boz Dağ) reaching an elevation of 2159 m. Inset shows the location of the study area (red box) in western Turkey and three main graben systems. Red line delineates the drainage divide. Quaternary basins near the crest line (Süzen *et al.* 2006) are shown as white areas. Black continuous line with grey shaded area marks the location of the swath profile shown in (**b**). Blue dots mark the positions where the field photographs in Figure 2 were taken. (**b**) Swath profile across Boz Dağ block parallel to the regional extension direction. Location of the profile is shown in (**a**). Note the pronounced topographic asymmetry, with the shallow-dipping Gediz detachment on the northern flank and the steep escarpment on the southern flank of the Boz Dağ block.

To quantify erosion rates, cosmogenic nuclides such as ^{10}Be can be used because the cosmogenic nuclide concentration of an eroding surface depends on the rate of erosion (Lal 1991; Granger *et al.* 1996; von Blanckenburg 2006). To date, however, only a few studies have applied cosmogenic nuclides to derive erosion rates in regions of active continental extension. In the Basin-and-Range Province, a few studies recently determined erosion rates in mountain ranges bounded by high-angle normal faults, and compared these rates with exhumation rates derived from low-temperature thermochronology (Densmore *et al.* 2009; Stock *et al.* 2009). For the Wasatch Mountains (Utah), relatively low ^{10}Be-based erosion rates of 70–170 mm ka^{-1} were determined in catchments draining the western range front, whereas catchments in the range centre erode at 170–790 mm ka^{-1} (Stock *et al.* 2009). The mean denudation rate of *c.* 0.2 mm a^{-1} is similar to the exhumation rates derived from low-temperature thermochronology (0.2–0.4 mm a^{-1}; Armstrong *et al.* 2003, 2004; Ehlers *et al.* 2003). Catchments in the Wassuk Range showed highly variable erosion rates between 70 and 630 mm ka^{-1} (Densmore *et al.* 2009), with peak rates approaching the long-term exhumation rate (Stockli *et al.* 2002; Densmore *et al.* 2009). In the Aegean region, no erosion rates derived from cosmogenic nuclides exist so far, although cosmogenic nuclides were used to date glacial deposits (e.g. in SW Turkey: Sarıkaya *et al.* 2008; Zahno *et al.* 2009) and bedrock fault scarps (e.g. Benedetti *et al.* 2002).

Here we present apatite and zircon (U–Th)/He and fission-track as well as cosmogenic ^{10}Be data from the actively extending Menderes Massif in western Turkey. As constrained by global positioning system (GPS) data, the present-day north–south extension rate across the Menderes Massif is 12–15 mm a^{-1} (Aktug *et al.* 2009). Our study area is located in the northern part of the central Menderes Massif, which includes the highest peak (Boz Dağ; 2159 m) of the entire massif (Fig. 1a). The Boz Dağ region also exhibits the highest local relief of the Menderes Massif and is characterized by a pronounced topographic asymmetry, with a gently dipping northern flank facing the Gediz Graben and a steep southern flank facing the Küçük Menderes Graben (Fig. 1b). The new data allow us to determine the exhumation of rocks and catchment-wide erosion rates in the Boz Dağ region and to place constraints on the slip rate and rotation of the shallow-dipping Gediz (or Alaşehir) detachment, which dominates the geomorphology of the northern flank of the Boz Dağ block (Figs 1b and 2a). In the following, we first introduce the geological setting of the central Menderes Massif and give a description of the collected samples, their preparation and analysis. After presentation of the results, we discuss the implications of our data for the tectonic and geomorphological evolution of the Boz Dağ region.

Geological and geomorphological setting of the central Menderes Massif

The central Menderes Massif consists of a nappe pile that formed during Late Cretaceous to Early Tertiary crustal shortening (Ring *et al.* 1999). The metamorphic rocks of the Bayındır and Boz Dağ nappes (Fig. 3; Ring *et al.* 1999; Gessner *et al.* 2001*a*,*b*) include mainly greenschist- to amphibolite-facies schists, paragneisses, deformed granitoids, and quartzites (Dora *et al.* 1990, 2001; Hetzel *et al.* 1998; Ring *et al.* 2001). In addition, there are minor amounts of phyllites and marbles (Bayındır nappe) and small eclogite bodies (Çine nappe) (Oberhänsli *et al.* 1997; Candan *et al.* 2001). Since the early or middle Miocene, NNE–SSW-directed bivergent extension of the Menderes Massif nappe pile led to the formation of two detachments with opposite dips, the Gediz and Büyük Menderes detachments (Hetzel *et al.* 1995*a*; Gessner *et al.* 2001*b*, 2013; Ring *et al.* 2003). The Gediz detachment is spectacularly exposed on the northern flank of the Boz Dağ block and dips *c.* 15° to the NNE (Fig. 2a). The greenschist-facies metasediments beneath the Gediz detachment show a mylonitic foliation, which dips gently to the north, and exhibit a well-developed stretching lineation plunging gently north to NE (Fig. 3a; Hetzel *et al.* 1995*b*; Emre 1996; Işık *et al.* 2003). Abundant kinematic indicators in the mylonites indicate a consistent top-to-the-NNE shear sense (Hetzel *et al.* 1995*b*; Işık *et al.* 2003). The ductile deformation was accompanied by the intrusion of two syntectonic granodiorites, SE of Salihli (Fig. 3) and south of Turgutlu, into the Bayındır nappe. U–Pb dating of the granodiorites yielded intrusion ages of 16.1 ± 0.2 Ma (Turgutlu granodiorite) and 15.0 ± 0.3 Ma (Salihli granodiorite), respectively (Glodny & Hetzel 2007). Between the northern rim of the exposed

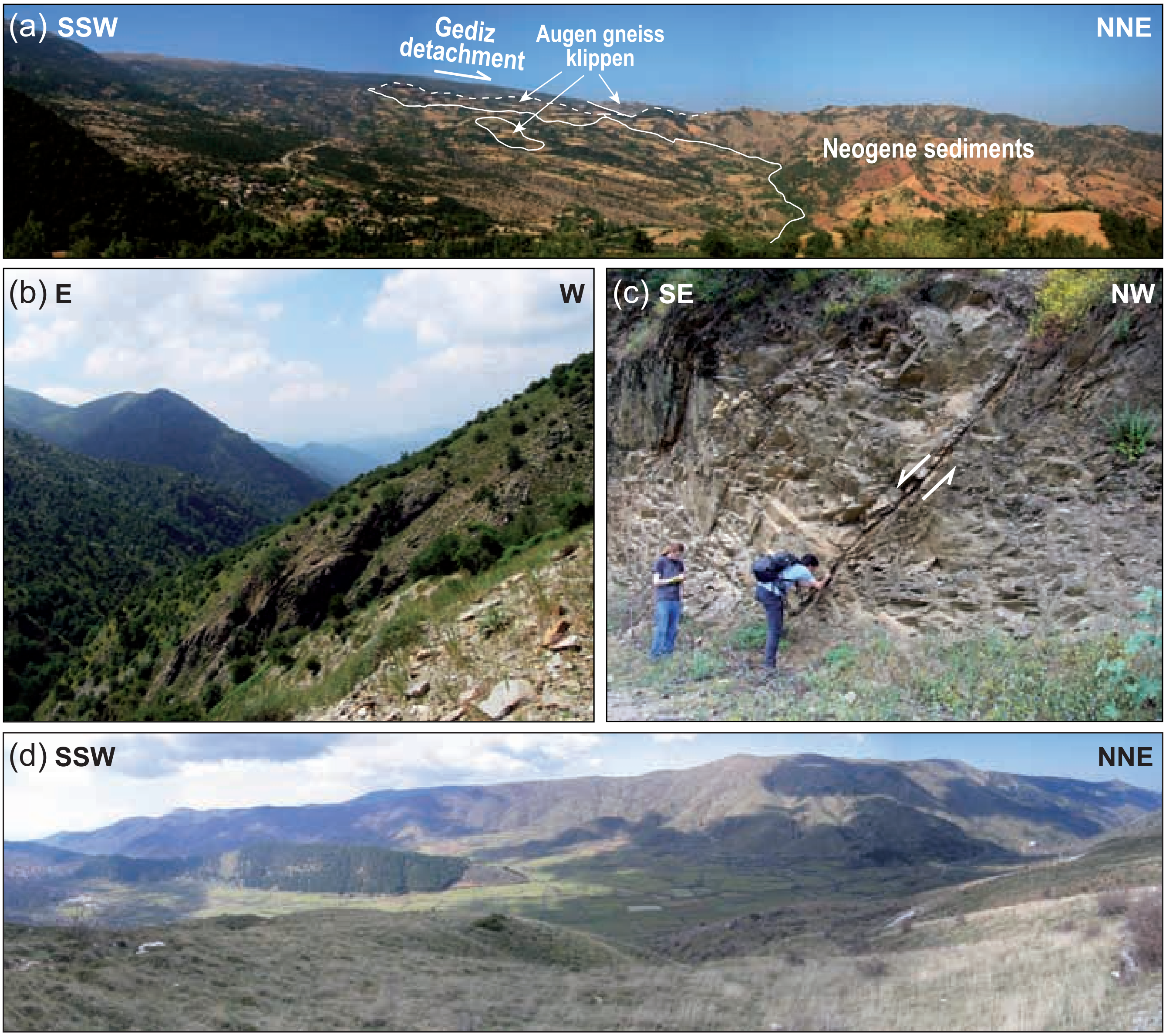

Fig. 2. (**a**) Northern flank of the Boz Dağ block with exposure of the *c.* 15°-dipping Gediz detachment fault. (**b**) Deeply incised valley on the southern flank of the Boz Dağ horst. (**c**) High-angle normal fault in schists of the Boz Dağ nappe on the southern flank of the Boz Dağ block. (**d**) High-altitude Quaternary basin west of Boz Dağ peak.

part of the Gediz detachment and the southern margin of the Gediz Graben, which is marked by high-angle normal faults, tilted Neogene strata are in tectonic contact with the detachment underneath (Figs 2a and 3; Seyitoğlu & Scott 1991; Bozkurt & Sözbilir 2004; Purvis & Robertson 2004, 2005; Sen & Seyitoğlu 2009). The spatial distribution of Early Miocene and Pliocene continental deposits in the hanging wall of the Gediz detachment indicates that during the preceding extensional history, high-angle normal faulting in the supradetachment basin shifted progressively northwards (e.g. Paton 1992; Seyitoğlu *et al.* 2002). In the hanging wall of the Gediz detachment there are also small klippen of augen gneiss that represent remnants of the Çine nappe, which is exposed in the eastern part of the Küçük Menderes Graben (Fig. 3a).

In the centre of the Boz Dağ block, where the synextensional foliation is still dominant, the shear sense changes to top-to-the-SSW (Hetzel *et al.* 1995*b*). On the steep southern flank of the Boz Dağ block that faces the Küçük Menderes Graben (Fig. 2b), high-angle normal faults are exposed (Fig. 2c; Rojay *et al.* 2005; Emre & Sözbilir 2007; Bozkurt *et al.* 2008). The normal faults formed in the Boz Dağ nappe schists, which show a mainly pre-extensional SSW-dipping foliation inherited from the earlier Alpine deformation (Fig. 3a; Hetzel *et al.* 1998). The southward dip of the foliation increases toward the Küçük Menderes Graben and reaches maximum values of 70–80° (Fig. 3a).

Characteristic geomorphological features of the Boz Dağ block include the pronounced topographic asymmetry and the location of the overall east–west-trending drainage divide close to the Küçük Menderes Graben (Fig. 1). As a consequence, streams flowing into the Gediz Graben have elongated catchments with their long axes parallel to the regional NNE–SSW extension direction (Fig. 3b). In contrast, the deeply incised basins draining the steep escarpment south of Boz Dağ are smaller and have an equidimensional shape

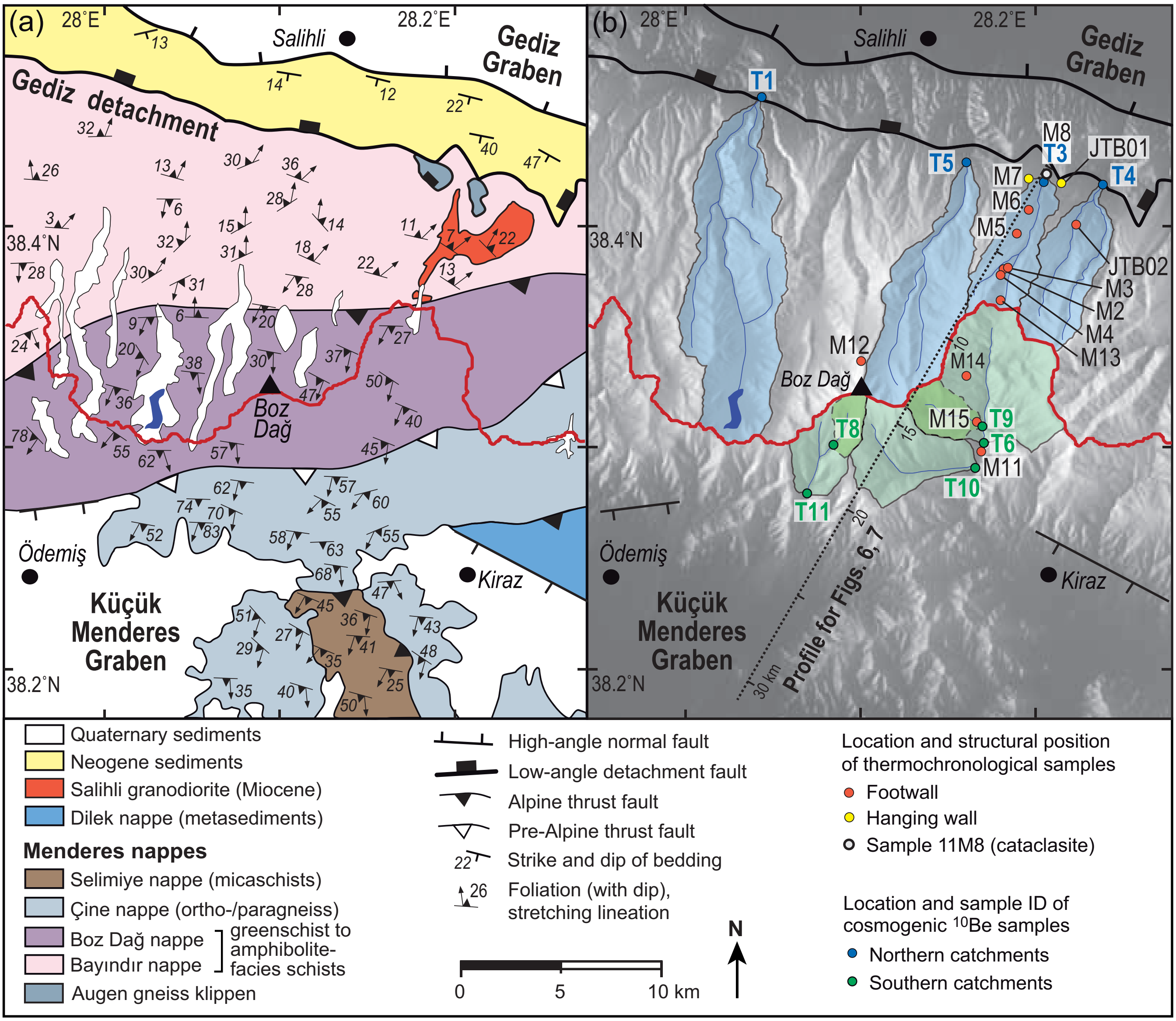

Fig. 3. (**a**) Geological map of the Boz Dağ region (modified from Hetzel *et al.* 1995*a*; Gessner *et al.* 2001*a*,*b*; Süzen *et al.* 2006). Orientations of foliation and stretching lineation are from Hetzel *et al.* (1995*a*,*b*, 1998). It should be noted that the foliation symbols do not differentiate between synextensional foliation, which dominates in the northern and central parts of the Boz Dağ region, and an older pre-extensional foliation, which occurs mainly in its southern part. (**b**) Shaded-relief map of the Boz Dağ region showing the location and number of samples for thermochronology and for the determination of ^{10}Be-derived catchment-wide erosion rates. The leading two sample identification numbers of the thermochronological and ^{10}Be samples are omitted in the figure for clarity (see Tables 1 and 5). Catchments draining toward the Gediz Graben are shaded in blue; catchments draining toward the Küçük Menderes Graben are shaded in green. Samples T8 and T9 were taken from subcatchments of the larger catchments T11 and T6, respectively.

(Fig. 3b). Near the drainage divide, internally drained, high-altitude basins filled with fluvial and lacustrine sediments of Quaternary age have developed (Figs 1a and 2d; Süzen *et al.* 2006), which are currently being drained again by northward flowing streams.

Several studies have documented that during past glaciations the landscapes of tectonically active Mediterranean mountains were shaped by glaciers (e.g. Hughes *et al.* 2006, 2011). In SW Turkey, glaciers were present during the last glacial maximum on Mount Sandıras (Sarıkaya *et al.* 2008) and on the Dedegöl Mountains (Zahno *et al.* 2009) at elevations above *c.* 1900 m and 1600 m, respectively. Although the northern slopes of Boz Dağ mountain may have contained very small glaciers, we did not find any evidence for the presence of glacial deposits. We attribute the weak glacial activity to the limited area available for the accumulation of snow and ice. The more pronounced impact of glaciers in other regions of SW Turkey can be explained by a higher elevation (almost 3000 m in the case of the Dedegöl Mountains) or a location close to the humidity source of the Mediterranean Sea (in the case of Mount Sandıras).

Methods and sample collection, preparation and analysis

Apatite and zircon (U–Th)/He thermochronology

The (U–Th)/He technique measures the amount of alpha particles (^{4}He) generated from the radioactive decay of uranium (^{238}U, ^{235}U), thorium (^{232}Th), and samarium (^{147}Sm) that become trapped in crystal lattices (Rutherford 1905; Zeitler *et al.* 1987; Lippolt *et al.* 1994).

Table 1. *Location and lithology of samples for low-temperature thermochronology*

Sample number	Latitude (°N) (WGS 84)	Longitude (°E) (WGS 84)	Elevation (m)	Lithology and structural position	Thermochronometers applied
10JTB01	38.4191	28.2151	560	Augen gneiss from klippe in hanging wall	AHe, AFT, ZHe
10JTB02	38.4005	28.2236	720	Mylonitic granodiorite, footwall	AHe, AFT, ZHe, ZFT
11M2	38.3804	28.1826	1550	Two-mica schist, footwall	AHe
11M3	38.3812	28.1850	1482	Mylonitic granodiorite, footwall	AHe, ZHe
11M4	38.3775	28.1806	1636	Two-mica schist, footwall	AHe
11M5	38.3963	28.1898	1201	Mylonitic granodiorite, footwall	AHe, ZHe
11M6	38.4073	28.1968	962	Mylonitic granodiorite, footwall	AHe, ZHe
11M7	38.4210	28.1964	708	Augen gneiss from klippe in hanging wall	AHe, AFT, ZHe
11M8	38.4205	28.2074	560	Cataclasite from detachment fault	AHe, ZHe
11M11	38.2987	28.1693	636	Two-mica schist, footwall	AHe, ZHe
11M12	38.3388	28.1009	1748	Two-mica schist, footwall	AHe
11M13	38.3667	28.1803	1540	Mylonitic granodiorite, footwall	AHe, AFT, ZHe
11M14	38.3326	28.1610	1324	Two-mica schist, footwall	AHe, ZHe
11M15	38.3119	28.1670	982	Two-mica schist, footwall	AHe, ZHe

AHe, apatite (U–Th)/He; ZHe, zircon (U–Th)/He; AFT, apatite fission track; ZFT, zircon fission track.

Alpha particles initially become trapped in the partial retention zone, a distinct temperature range where ^{4}He is partially diffused and retained (e.g. Wolf *et al.* 1998; Ehlers & Farley 2003). At temperatures below the partial retention zone, ^{4}He is predominantly retained and the measured amount of ^{4}He relative to the parent isotopes represents a cooling age. Apatite and zircon are the most commonly used minerals for (U–Th)/He thermochronology; the relatively high diffusivity of helium in these phases allows dating of near-surface thermal events. The partial retention temperatures for apatite (AHe) and zircon (ZHe) are *c.* 40–85 °C and *c.* 150–190 °C, respectively, and the typical closure temperatures are *c.* 70 °C and *c.* 180 °C, respectively (Wolf *et al.* 1996; Farley 2000; Ehlers & Farley 2003; Reiners *et al.* 2004; Reiners & Brandon 2006; Flowers *et al.* 2007; Herman *et al.* 2007).

For our study, we collected 14 bedrock samples from the Boz Dağ region for (U–Th)/He thermochronology (Table 1; Fig. 3b). The majority of the samples were collected along a NNE–SSW transect parallel to the regional extension direction. North of the crestline of the Boz Dağ block, we collected eight samples from the footwall of the Gediz detachment, with five samples from the Salihli granodiorite (10JTB02, 11M3, 11M5, 11M6, 11M13) and three samples (11M2, 11M4, 11M12) from the two-mica schists of the Boz Dağ and Bayındır nappes. In addition, we took a cataclasite sample (11M8) from the Gediz detachment and two samples from the augen gneiss klippen (10JTB01, 11M7) located in its hanging wall. On the southern flank of the Boz Dağ, we collected three samples (11M11, 11M14, 11M15) from the two-mica schist of the Boz Dağ nappe (Fig. 3b).

From all 14 samples, AHe ages were obtained; for 11 samples, we also determined ZHe ages (Table 1). Apatite and zircon crystals were concentrated using standard mineral separation procedures (crushing, sieving and gravity, density and magnetic separation). Crystals were then hand-picked using a stereomicroscope and selected under 200× magnification with polarized light. Clear, intact, euhedral apatite and zircon single crystals free of visible inclusions were used when possible for single-grain aliquots. The dimensions of single crystals were measured with a length-calibrated microscope to determine the shape factor for alpha-ejection correction (Farley *et al.* 1996) and the single crystals were loaded into Pt tubes for He analyses.

The AHe and ZHe analyses were carried out at the Helium Geochronology laboratory at the University of Göttingen. Extraction of retained helium from selected single-grain apatite and zircon aliquots was performed by heating the encapsulated grains in vacuum using an IR laser at a temperature of *c.* 900 °C. The extracted gas was then purified by an SAES Ti–Zr getter, separating helium from impurities present in the system. A Hiden Hal-3F/PIC triple-filter quadrupole mass spectrometer measured the ^{4}He content. For measurements of the alpha-emitting elements U, Th and Sm, the degassed crystals were dissolved and spiked with calibrated ^{233}U and ^{230}Th solutions. Apatites were dissolved in 2% ultrapure HNO_3 (+ 0.05% HF) at room temperature in an ultrasonic bath. Zircons were dissolved in Teflon® bombs containing a mixture of 48% HF and 65% HNO_3 at 220 °C for 5 days. The actinide and Sm concentrations were determined by inductively coupled plasma mass spectrometry (ICP-MS) using the isotope dilution method with a Perkin Elmer Elan DRC II system equipped with an APEX micro-flow nebulizer. Errors for the single-grain AHe and ZHe analyses are attributed to uncertainties in the He, U, Th, and Sm measurements and the estimated uncertainty of the Ft correction factor (Tables 2 and 3).

Apatite and zircon fission-track analysis

Four of the samples collected for (U–Th)/He analyses (10JTB01, 10JTB02, 11M7, 11M13) were used for apatite fission-track (AFT) analysis (Table 1). For one of these samples (10JTB02), we also determined a zircon fission-track (ZFT) age. Similar to the (U–Th)/He method, fission tracks are partially retained in the partial annealing zones of apatite and zircon, which are in the range of 60–120 °C and 190–380 °C, respectively (e.g. Wagner & van den Haute 1992; Rahn *et al.* 2004). Corresponding closure temperatures for typical apatite and zircon fission-track samples are *c.* 110 °C and *c.* 240 °C, respectively (e.g. Gleadow & Duddy 1981; Wagner & van den Haute 1992).

For the fission-track analysis of our study, apatites and zircons were embedded in epoxy and PFA Teflon™, respectively, and afterwards ground and polished to expose internal grain surfaces. Apatite mounts were etched with 5M HNO_3 for 20 s at 20 °C and zircon mounts were etched with a eutectic melt of KOH–NaOH for 60 h at 215 °C (Zaun & Wagner 1985). Samples were irradiated with thermal neutrons at the FRM-II reactor facility in Garching (Technical University Munich, Germany). To reveal induced tracks, mica external detectors were etched with 40% HF at 20 °C for 40 min. Fission-track counting was carried out on an Olympus BX-51 microscope under 1000× magnification using

Table 2. *Results of apatite (U–Th)/He geochronology*

Sample number	Aliquot number	He		^{238}U			^{232}Th				Sm			Ejection correction (Ft)	Uncorr. He age (Ma)	Ft-corr. He age (Ma)		Sample age (Ma)	
		Vol. (10^{-9}cm^3)	1σ (%)	Mass (ng)	1σ (%)	Conc. (ppm)	Mass (ng)	1σ (%)	Conc. (ppm)	Th/U ratio	Mass (ng)	1σ (%)	Conc. (ppm)				2σ		2SE
10JTB01	1	0.004	18.1	0.046	2.3	13.4	0.012	3.3	3.5	0.26	0.261	7.2	76	0.699	0.72	1.02	0.38	0.8	±0.2
	2	0.006	13.8	0.162	1.9	37.4	0.014	3.1	3.2	0.09	0.389	7.4	90	0.677	0.31	0.46	0.13		
	3	0.005	18.3	0.049	2.2	13.8	0.027	2.8	7.6	0.55	0.387	7.8	108	0.689	0.67	0.97	0.37		
10JTB02	1	0.008	7.8	0.027	2.7	15.4	0.027	2.7	15.5	1.01	0.330	5.4	188	0.679	1.73	2.55	0.48	2.5	±0.1
	2	0.013	5.7	0.057	2.1	27.7	0.026	2.7	12.7	0.46	0.328	5.5	160	0.641	1.62	2.52	0.40		
	3	0.007	7.1	0.033	2.4	27.7	0.017	2.9	14.4	0.52	0.174	5.5	145	0.646	1.53	2.38	0.43		
11M2	1	0.001	34.1	0.007	10.5	5.6	0.002	5.1	1.7	0.30	0.150	26.5	113	0.689	1.24	1.80	1.28	2.5	±0.9
	2	0.002	34.2	0.013	6.3	7.3	0.001	10.6	0.7	0.09	0.202	27.8	117	0.708	0.94	1.32	0.93		
	3	0.003	21.0	0.008	10.0	7.1	0.003	4.6	2.8	0.40	0.035	28.8	29	0.664	2.85	4.30	2.00		
11M3	1	0.008	13.5	0.038	2.7	18.9	0.022	2.9	10.8	0.57	0.337	29.2	167	0.661	1.45	2.19	0.64	2.0	±0.2
	2	0.006	16.0	0.036	2.8	25.3	0.031	2.7	21.5	0.85	0.305	30.0	214	0.654	1.09	1.67	0.57		
	3	0.006	10.5	0.026	3.9	18.5	0.026	2.8	19.0	1.02	0.258	11.9	187	0.671	1.47	2.20	0.52		
11M4	1	0.008	13.5	0.012	6.9	10.1	0.002	5.5	1.7	0.17	0.105	14.6	91	0.659	5.28	8.01	2.51	8.2	±0.3
	2	0.006	15.1	0.008	10.2	12.4	0.002	6.5	2.5	0.20	0.064	14.2	97	0.658	5.54	8.42	3.07		
11M5	1	0.102	3.9	0.572	1.8	147.2	0.025	2.8	6.5	0.04	0.831	13.6	214	0.768	1.45	1.89	0.21	1.7	±0.2
	2	0.003	21.9	0.020	4.2	6.8	0.010	3.4	3.5	0.52	0.468	10.4	161	0.768	0.93	1.22	0.55		
	3	0.051	5.0	0.287	1.8	93.0	0.006	4.1	1.8	0.02	0.667	11.5	216	0.686	1.43	2.08	0.30		
	4	0.009	12.8	0.065	2.2	33.7	0.016	3.1	8.1	0.24	0.453	17.6	235	0.626	1.06	1.69	0.48		
11M6	1	0.010	12.7	0.080	2.0	41.7	0.013	3.2	6.7	0.16	0.493	12.0	258	0.680	0.97	1.42	0.39	1.9	±0.2
	2	0.018	8.6	0.100	1.9	52.3	0.011	3.3	5.9	0.11	0.499	12.3	261	0.647	1.41	2.18	0.45		
	3	0.008	12.3	0.049	2.3	45.1	0.015	3.1	13.5	0.30	0.342	12.6	315	0.648	1.27	1.96	0.53		
11M7	1	0.044	5.1	0.182	1.9	92.3	0.004	4.4	2.0	0.02	0.346	13.0	175	0.703	1.94	2.76	0.39	2.9	±0.8
	2	0.002	33.6	0.021	3.7	18.6	0.002	5.5	1.7	0.09	0.092	13.8	81	0.646	0.69	1.07	0.73		
	3	0.058	5.2	0.121	1.9	27.1	0.004	4.7	0.8	0.03	0.739	13.9	166	0.727	3.76	5.18	0.71		
	4	0.008	12.7	0.028	3.0	15.1	0.016	3.0	8.9	0.59	0.291	15.1	158	0.711	1.88	2.64	0.72		
11M8	1	0.003	28.5	0.006	12.9	1.2	0.009	3.5	1.7	1.43	0.199	14.2	39	0.774	2.30	2.97	1.77	3.0	±1.8
11M11	1	0.005	13.8	0.012	8.2	9.5	0.005	4.9	4.1	0.43	0.200	29.8	157	0.658	2.94	4.47	1.47	2.6	±2.6
	2	0.001	26.5	0.003	39.1	2.3	0.070	2.5	56.3	24.10	0.068	29.3	54	0.652	0.48	0.73	0.40		
11M12	1	0.012	9.1	0.022	4.6	6.1	0.007	4.4	2.1	0.34	0.263	26.1	74	0.719	3.83	5.33	1.17	5.7	±1.7
	2	0.003	17.9	0.009	10.7	3.6	0.001	13.2	0.3	0.09	0.162	25.6	62	0.766	2.28	2.97	1.22		
	3	0.011	9.1	0.012	6.2	3.4	0.000	0.0	0.0	0.00	0.261	8.3	75	0.781	6.81	8.72	1.91		
11M13	1	0.006	14.9	0.027	3.4	20.7	0.020	2.9	15.6	0.75	0.338	24.6	261	0.667	1.43	2.15	0.69	2.1	±0.03
	2	0.008	13.6	0.035	2.8	17.4	0.034	2.7	16.8	0.97	0.538	25.2	265	0.696	1.43	2.05	0.60		
	3	0.007	14.4	0.042	2.6	30.0	0.017	3.0	12.2	0.41	0.315	25.9	224	0.602	1.25	2.07	0.66		
11M14	1	0.001	26.2	0.005	23.0	2.4	0.004	5.8	1.8	0.76	0.079	25.1	39	0.702	1.71	2.43	1.54	3.5	±1.5
	2	0.004	16.6	0.007	11.2	2.4	0.006	4.1	2.0	0.84	0.093	8.6	33	0.756	3.47	4.59	1.73		
11M15	1	0.001	33.6	0.003	34.4	1.0	0.002	6.5	0.5	0.55	0.178	22.6	52	0.707	2.23	3.16	2.55	3.7	±0.4
	2	0.003	21.1	0.004	23.1	1.6	0.006	5.0	2.1	1.33	0.170	22.2	60	0.721	3.16	4.39	2.26		
	3	0.003	21.8	0.007	15.4	2.3	0.005	5.4	1.6	0.67	0.137	21.8	44	0.748	2.59	3.47	1.73		

Ejection correction (Ft) is the correction factor for alpha-ejection (according to Farley *et al.* 1996 and Hourigan *et al.* 2005). Uncertainty of the single-grain ages includes both the analytical uncertainty and the estimated uncertainty of the ejection correction. Sample age is the unweighted average age of all Ft-corrected (U–Th)/He ages. The results of aliquots that yielded markedly older ages than the other aliquots of a sample were considered to be outliers and are not shown.

Table 3. *Results of zircon (U–Th)/He geochronology*

Sample number	Aliquot number	He		^{238}U			^{232}Th			Th/U ratio	Ejection correction (Ft)	Uncorr. He age (Ma)	Ft-corr. He age (Ma)		Sample age (Ma)	
		Vol. (10^{-9} cm^3)	1σ (%)	Mass (ng)	1σ (%)	Conc. (ppm)	Mass (ng)	1σ (%)	Conc. (ppm)					2σ (Ma)		2SE (Ma)
10JTB01	1	2.367	1.7	1.272	1.8	399	0.276	2.4	87	0.22	0.727	14.65	20.15	1.91	19.5	±0.9
	2	1.627	1.8	0.963	1.8	445	0.080	2.4	37	0.08	0.721	13.71	19.02	1.85		
	3	1.766	1.8	1.021	1.8	290	0.250	2.4	71	0.25	0.785	13.53	17.24	1.40		
	4	5.173	1.7	2.405	1.8	316	0.291	2.4	38	0.12	0.804	17.31	21.52	1.63		
10JTB02	1	0.760	1.9	4.212	1.8	1528	0.249	2.4	91	0.06	0.762	1.47	1.94	0.43	2.0	±0.1
	2	0.985	1.9	5.930	1.8	2840	0.378	2.4	181	0.06	0.759	1.36	1.79	0.16		
	3	0.749	1.9	3.947	1.8	1432	0.321	2.4	116	0.08	0.741	1.54	2.08	0.19		
	4	2.553	1.7	13.091	1.8	2859	0.751	2.4	164	0.06	0.793	1.60	2.01	0.16		
11M3	1	0.801	2.1	2.228	1.8	758	0.347	2.4	118	0.16	0.731	2.87	3.93	0.38	3.3	±0.3
	2	0.806	2.0	2.754	1.8	872	0.417	2.4	132	0.15	0.740	2.34	3.16	0.30		
	3	1.012	2.0	3.922	1.8	1388	0.355	2.4	126	0.09	0.737	2.09	2.84	0.27		
11M5	1	0.695	2.1	2.220	1.8	613	0.408	2.4	113	0.18	0.750	2.49	3.31	0.30	3.6	±0.2
	2	1.278	1.9	3.688	1.8	752	0.531	2.4	108	0.14	0.774	2.78	3.59	0.30		
	3	2.262	1.8	5.804	1.8	967	1.114	2.4	186	0.19	0.778	3.09	3.97	0.33		
11M6	1	0.193	3.2	0.915	1.8	385	0.258	2.4	108	0.28	0.723	1.64	2.27	0.25	2.2	±0.1
	2	0.163	3.6	0.853	1.8	344	0.254	2.4	102	0.30	0.718	1.47	2.06	0.24		
	3	1.579	1.9	7.370	1.8	1791	0.554	2.4	135	0.08	0.760	1.75	2.30	0.20		
11M7	1	4.341	1.7	1.849	1.8	325	0.138	2.4	24	0.07	0.789	19.09	24.20	1.93	20.7	±1.8
	2	4.553	1.7	2.594	1.8	527	0.142	2.4	29	0.05	0.776	14.35	18.49	1.53		
	3	6.444	1.7	3.456	1.8	609	0.182	2.4	32	0.05	0.789	15.24	19.33	1.54		
11M8	1	2.759	1.8	1.737	1.8	462	0.127	2.4	34	0.07	0.742	12.93	17.41	1.60	18.4	±1.3
	2	5.991	1.7	3.237	1.8	528	0.152	2.4	25	0.05	0.784	15.15	19.32	1.56		
	3	0.485	2.4	1.938	1.8	274	0.416	2.4	59	0.21	0.804	1.97	2.45	0.20	*2.5**	*0.2**
11M11	1	1.740	1.8	1.582	1.8	389	0.613	2.4	151	0.39	0.765	8.35	10.91	0.93	9.7	±0.9
	2	1.447	1.8	1.526	1.8	500	0.143	2.4	47	0.09	0.743	7.68	10.34	0.95		
	3	0.446	2.3	0.615	1.8	237	0.156	2.4	60	0.25	0.722	5.67	7.85	0.79		
11M13	1	1.380	1.9	4.252	1.8	844	0.495	2.4	98	0.12	0.778	2.62	3.37	0.28	3.9	±0.4
	2	0.802	2.1	2.367	1.8	798	0.483	2.4	163	0.20	0.735	2.68	3.64	0.35		
	3	0.635	2.2	1.528	1.8	565	0.256	2.4	94	0.17	0.727	3.31	4.56	0.45		
11M14	1	0.330	2.4	0.708	1.8	233	0.184	2.4	61	0.26	0.736	3.64	4.94	0.49	6.4	±1.2
	2	0.949	2.0	1.765	1.8	591	0.571	2.4	191	0.32	0.736	4.14	5.63	0.53		
	3	0.628	1.9	0.761	1.8	307	0.243	2.4	98	0.32	0.724	6.35	8.77	0.85		
11M15	1	0.566	5.0	0.879	1.8	101	0.620	2.4	71	0.71	0.805	4.57	5.68	0.68	8.1	±1.3
	2	2.192	1.8	1.879	1.8	245	0.633	2.4	83	0.34	0.806	8.95	11.09	0.84		
	3	0.838	2.1	1.349	1.8	283	0.390	2.4	82	0.29	0.773	4.81	6.22	0.54		
	4	2.179	1.7	2.249	1.8	611	1.128	2.4	307	0.50	0.748	7.17	9.59	0.85		

Ejection correction (Ft) is the correction factor for alpha-ejection (according to Farley *et al.* 1996 and Hourigan *et al.* 2005). The uncertainty of the single-grain ages includes both the analytical uncertainty and the estimated uncertainty of the ejection correction. Sample age is the unweighted average age of all Ft-corrected (U–Th)/He ages.
*Details on interpretation of data from sample 11M8 are given in main text.

Table 4. *Results from apatite and zircon fission-track analyses*

Sample number	Mineral	Number of grains	ρ_s	n_s	ρ_i	n_i	ρ_d	n_d	$P(\chi^2)$ (%)	Central age* ±2σ (Ma)	D_{par}	U (ppm)
10JTB01	Apatite	25	1.527	83	7.838	426	8.306	3334	20	18.0±4.9	1.4±0.1	12
10JTB02	Apatite	25	0.308	17	11.443	631	8.295	3334	52	2.6±1.3	1.4±0.1	18
10JTB02	Zircon	20	28.081	360	95.008	1218	3.992	2468	0	6.4±0.9	–	313
11M7	Apatite	25	1.236	62	10.484	526	8.328	3334	49	11.2±3.3	1.3±0.1	17
11M13	Apatite	20	0.224	8	9.314	332	8.317	3334	36	2.3±1.7	1.4±0.1	15

ρ_s, spontaneous track density (10^5 tracks cm^{-2}); n_s, number of counted spontaneous tracks; ρ_i, induced track density (10^5 tracks cm^{-2}); n_i, number of counted induced tracks; ρ_d, dosimeter track density (10^5 tracks cm^{-2}); n_d, number of tracks counted on the dosimeter; $P(\chi^2)$, probability of obtaining chi-squared value (χ^2) for n degrees of freedom (where n is the number of crystals minus one); D_{par}, etch pit diameter of fission tracks, averaged from four measurements per analysed grain with their standard deviation.
*AFT ages were calculated using the zeta calibration method (Hurford & Green 1983), glass dosimeter IRMM540R, and a zeta value of 229±12 a cm^{-2} calculated with Durango apatite standards. ZFT ages were calculated using the zeta calibration method, glass dosimeter IRMM541, and a zeta value of 109±3 a cm^{-2} calculated with Fish Canyon zircon standards.

Table 5. *^{10}Be concentrations, production rates, and catchment-wide erosion rates in the central Menderes Massif, Turkey*

Sample number	Latitude (°N) (WGS 84)	Longitude (°E) (WGS 84)	Elevation of sample (m)	Mean catchment elevation (m)	Mean hillslope angle of catchment (deg.)	Topographic shielding	^{10}Be concentration* (10^4 at g^{-1})	Production rate		Erosion rate† (mm ka^{-1})	Internal 1σ error (mm ka^{-1})	External 1σ error (mm ka^{-1})	Time scale (ka)
								Spallation (at g^{-1} a^{-1})	Muons (at g^{-1} a^{-1})				
11T1	38.4580	28.0447	190	1077	19.8	0.9836	9.66 ± 0.42	9.84	0.260	85.7	±3.8	±7.4	7.0
11T3	38.4205	28.2074	565	1372	16.8	0.9924	11.36 ± 0.59	12.39	0.286	87.6	±4.6	±8.1	6.9
11T4	38.4182	28.2389	295	1331	21.9	0.9824	5.43 ± 0.29	11.90	0.282	181	±10	±17	3.3
11T5	38.4286	28.1610	375	1450	22.4	0.9802	12.19 ± 0.42	12.97	0.293	85.0	±3.0	±7.1	7.1
11T6	38.3012	28.1693	645	1432	25.0	0.9778	3.11 ± 0.20	12.73	0.292	336	±22	±33	1.8
11T8	38.2990	28.0835	915	1496	28.4	0.9660	2.47 ± 0.19	13.18	0.298	436	±34	±47	1.4
11T9	38.3076	28.1685	720	1426	24.0	0.9809	5.75 ± 0.51	12.72	0.291	180	±16	±21	3.3
11T10	38.2889	28.1640	570	1217	23.2	0.9812	2.76 ± 0.30	10.89	0.272	334	±37	±44	1.8
11T11	38.2781	28.0698	594	1185	24.5	0.9774	1.97 ± 0.18	10.58	0.269	459	±42	±54	1.3

The topographic shielding factors were calculated using a 30 m Aster Digital Elevation Model and the Matlab script of G. Balco (http://depts.washington.edu/cosmolab/shielding.m). The ^{10}Be production rates were calculated with the CRONUS-Earth ^{10}Be–^{26}Al calculator, version 2.2 (Balco *et al.* 2008; http://hess.ess.washington.edu), using the time-invariant production rate scaling model of Lal (1991) and Stone (2000) with the constant file version 2.2.1 of the online calculator. The time over which the erosion rate integrates is calculated by dividing the absorption depth scale of 60 cm by the erosion rate.

*Blank-corrected ^{10}Be concentrations. Propagated analytical errors (1σ) include the error based on counting statistics and the error of the blank correction. ^{10}Be concentrations were measured at ETH Zurich and are normalized to the secondary standard S2007N with a nominal $^{10}Be/^{9}Be$ ratio of 28.1×10^{-12} (Kubik & Christl 2010).

†Erosion rates were calculated with the CRONUS-Earth ^{10}Be–^{26}Al calculator, version 2.2 (Balco *et al.* 2008; http://hess.ess.washington.edu). Internal uncertainties include the errors from the counting statistics and the blank correction, whereas external uncertainties also include the systematic uncertainty of the sea-level high-latitude production rate. It should be noted that the 2.7% error associated with the $^{10}Be/^{9}Be$ ratio of the standard S2007N is also included in the external uncertainty. For the calculation of the catchment-wide erosion rates, we used a density of 2.5 g cm^{-3} and the mean elevation of the respective catchments.

dry objectives. Samples were dated with the external detector method (e.g. Naeser 1978) using Zeta values of 229 ± 12 and 109 ± 3 a cm^{-2} for apatite and zircon, respectively. The kinetic properties of single-grain apatites were estimated via measurement of D_{par} values, which is the length of the etch pit parallel to the crystallographic *c*-axis (Burtner *et al.* 1994). The results from AFT and ZFT analyses are summarized in Table 4.

Catchment-wide erosion rates from cosmogenic ^{10}Be

Spatially averaged erosion rates for river catchments can be determined from the ^{10}Be concentration in sand samples taken from active streams (e.g. Granger *et al.* 1996; von Blanckenburg 2006). The approach assumes that the sediment in the stream channels is well mixed, that nuclide production in the catchment equals the outflux of nuclides via erosion and radioactive decay, and that erosion is uniform through time (e.g. Bierman & Steig 1996; von Blanckenburg 2006). Erosion rates determined with cosmogenic nuclides integrate over the time interval needed to remove a *c.* 60 cm thick layer from the surface: commonly a period of 10^3–10^5 years (e.g. von Blanckenburg 2006).

To quantify spatially integrated erosion rates in the Boz Dağ block, we took stream sediment samples at the outlets of nine catchments (Fig. 3b). Four of these samples were collected from small streams that drain the gently dipping northern side of the Boz Dağ block and flow into the Gediz Graben. The position of these samples at the boundary between the metamorphic rocks and the Neogene sediments ensures that the sediment source area encompasses only metamorphic rocks and cataclasites but not the Neogene sediments. The remaining five samples were taken from catchments located on the steep southern side of the Boz Dağ horst (Fig. 3b). Two of these samples (11T8, 11T9) were taken from subcatchments of larger catchments (Fig. 3b). The size of the sampled catchments ranged from 4 to 64 km^2.

The 250–500 μm grain size fraction of the stream sediments obtained by sieving in the field was split into a magnetic and a non-magnetic fraction using a Frantz magnetic separator. This was followed by one etching step in 6M HCl, three to four etching steps in diluted HF–HNO_3 in a heated ultrasonic bath (Kohl & Nishiizumi 1992), and two alternating etching steps in aqua regia and 8M HF to obtain pure quartz (Goethals *et al.* 2009). After addition of *c.* 0.3 mg of Be-carrier, the quartz samples were dissolved and Be was separated by successive anion and cation exchange columns, and precipitated at pH 8–9 as $Be(OH)_2$. Following the transformation to BeO at 1000 °C and target preparation, ^{10}Be was analysed at the accelerator mass spectrometry (AMS) facility of ETH Zurich (Kubik & Christl 2010). The blank-corrected ^{10}Be concentrations reported in Table 5 are normalized to the secondary ETH standard S2007N, which has a nominal $^{10}Be/^{9}Be$ ratio of 28.1×10^{-12} (Kubik & Christl 2010) considering the ^{10}Be half-life of 1.387 Ma (Chmeleff *et al.* 2010; Korschinek *et al.* 2010). The secondary standard has been in use since 2010 and has been calibrated to the primary standard ICN 01-5-1 (Nishiizumi *et al.* 2007; Kubik & Christl 2010).

Results

Apatite and zircon (U–Th)/He and fission-track analysis

The dataset obtained from the thermochronological samples reveals a distinct grouping of ages between the footwall and hanging wall of the Gediz detachment as well as between the northern and southern flanks of the Boz Dağ block. North of the drainage divide, samples collected from the mylonitized Salihli granodiorite and the two-mica schist in the footwall of the Gediz detachment yield AHe and ZHe ages in the range of 2.5–1.7 Ma and 3.9–2.0 Ma,

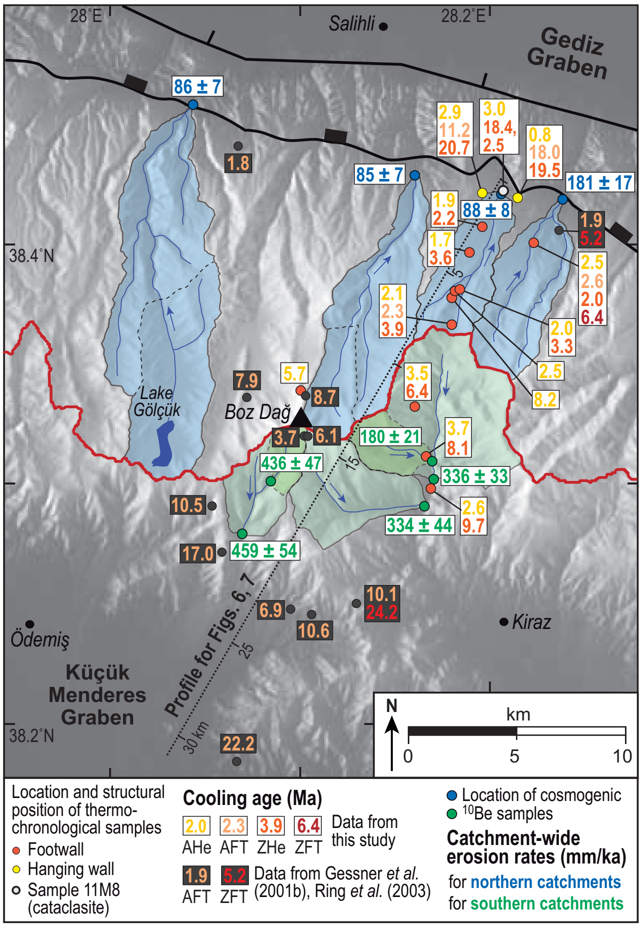

Fig. 4. Shaded-relief map of study area with results of thermochronological and cosmogenic nuclide analyses. Also shown are fission-track ages from Gessner *et al.* (2001*b*) and Ring *et al.* (2003). Fine dashed lines in catchments sampled for 11T1 and 11T5 mark the northern boundaries of the internal basins.

respectively (Fig. 4; Tables 2 and 3). Sample 11M4 shows an AHe age of 8.2 ± 0.3 Ma, which we consider as an outlier because two samples taken nearby (11M2, 11M3) show AHe ages of 2.5 ± 0.9 and 2.0 ± 0.2 Ma. From two samples (11M13, 10JTB02), AFT ages of 2.6 ± 1.3 and 2.3 ± 1.7 Ma as well as a ZFT age (10JTB02) of 6.4 ± 0.9 Ma were obtained (Table 4). It should be noted that although the nominal value of the ZHe age of sample 10JTB02 is younger than the AHe and AFT ages, the ages overlap within their error range (Tables 2–4). The similarity of the ages can be explained by fast exhumation. Samples from the augen gneiss klippen in the detachment hanging wall (11M7, 10JTB01) yielded young AHe ages of 2.9 ± 0.8 and 0.8 ± 0.2 Ma but high AFT ages (11.2 ± 3.3 and 18.0 ± 4.9 Ma) and ZHe ages (20.7 ± 1.8 and 19.5 ± 0.9 Ma). For the cataclasite sample 11M8, an AHe age of 3.0 ± 1.8 Ma was obtained from a single apatite crystal (Table 2) and a ZHe age of 2.5 ± 0.2 Ma from one of three analysed aliquots (Table 3). The two other aliquots from the cataclasite sample yielded significantly older ZHe ages with a mean value of 18.4 ± 1.3 Ma. The sample near Boz Dağ peak (11M12) yielded an AHe age of 5.7 ± 1.7 Ma. Samples taken from the footwall south of the drainage divide (11M11, 11M14, 11M15) show AHe and ZHe ages of 3.7–2.6 Ma and 9.7–6.4 Ma, respectively (Fig. 4).

Catchment-wide erosion rates from cosmogenic ^{10}Be

Catchment-wide erosion rates were calculated from the blank-corrected ^{10}Be concentrations with the CRONUS-Earth online calculator (Balco *et al.* 2008; version 2.2; http://hess.ess.washington.edu) using the time-invariant production rate scaling model of Lal (1991) and Stone (2000). To account for the shielding of the cosmic rays by the surrounding topography, a shielding factor was calculated for each catchment with G. Balco's Matlab script (http://depts.washington.edu/cosmolab/shielding.m) and a digital elevation model with a resolution of 30 m (ASTER GDEM; http://www.gdem.aster.ersdac.or.jp). The integration times for our samples range from *c.* 1.3 to *c.* 7.1 ka (Table 5). The results (Table 5) show that catchments draining to the north generally erode at significantly lower rates than catchments draining to the south (Fig. 4). Three of the catchments draining toward the Gediz Graben erode at rates between 85 and 90 mm ka^{-1}. The erosion rates of the two western catchments 11T1 and 11T5 change only slightly to lower values of 80 ± 8 mm ka^{-1} and 83 ± 7 mm ka^{-1}, respectively, if the area of the internal basins is excluded from the calculation. For the easternmost of the northern catchments (11T4), a higher erosion rate of 181 ± 17 mm ka^{-1} was obtained. In contrast, the steep southern catchments erode at rates between 330 and 460 mm ka^{-1}, with two smaller subcatchments eroding at 436 ± 47 and 180 ± 21 mm ka^{-1}, respectively (Fig. 4). Finally, we note that the use of other production rate scaling models implemented in the CRONUS-Earth online calculator (Dunai 2001; Lifton *et al.* 2005; Desilets *et al.* 2006) would result in erosion rates that are slightly lower (at most 11%) than those reported in Table 5.

Data interpretation and discussion

Slip rate of Gediz detachment fault

The subset of our low-temperature thermochronological data from the northern flank of the Boz Dağ block allows the slip rate of the Gediz detachment fault to be determined under the assumptions that (1) isotherms are subhorizontal and stationary, (2) the fault dip has not changed significantly, and (3) footwall cooling is caused solely by tectonic denudation (e.g. Foster & John 1999; Brady 2002; Brichau *et al.* 2006, 2008). Concerning the first assumption, thermal models have shown that especially shallower isotherms are not significantly deflected by slip on a detachment fault even for slip rates as high as 5 or 10 mm a^{-1} (Ketcham 1996), with the consequence that cooling rates and slip rates are probably not strongly affected by thermal effects (e.g. Brichau *et al.* 2006). The second assumption of a negligible rotation of the Gediz detachment during the last few million years is supported by the sedimentological record of the Gediz Graben, which indicates (based on the sedimentary facies and the inferred distal position of depocentres) that the detachment was probably not steeper than 30° since its initiation in the Early Miocene (Purvis & Robertson 2004, 2005; Oner & Dilek 2011). Furthermore, the formation and subsequent preservation of the high-altitude sedimentary basins near the drainage divide (Figs 1 and 2d) indicates that there was a southward tilt of the Boz Dağ block by a few degrees because the northward flow of water had to be interrupted for basin formation (Süzen *et al.* 2006). This implies that the detachment now has a more shallow dip than in the past. On the other hand, however, the amount of tilting cannot have exceeded a few degrees because otherwise the basins would have been captured by the southward flowing streams that drain the Boz Dağ region (Süzen *et al.* 2006). Hence, although the Boz Dağ block was tilted to a minor extent causing the detachment to have a more shallow dip than in the past, a rotation of more than a few degrees seems unlikely. The validity of

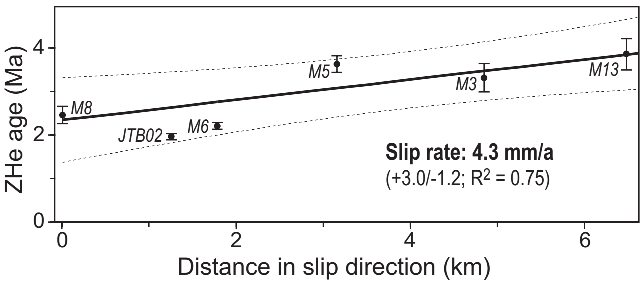

Fig. 5. Slip rate determination for the Gediz detachment from six ZHe ages that are plotted versus distance in slip direction.

the third assumption is supported by the relatively low ^{10}Be-derived erosion rates, which are between *c.* 80 and *c.* 180 mm ka^{-1} on the northern flank of Boz Dağ (Fig. 4). If these rates are representative of the last few million years, this implies that no more than a few hundred metres of rock have been removed by erosion. This value is an order of magnitude smaller than the 4–5 km of exhumation indicated by the ZHe ages (see next section).

To constrain the slip rate of the Gediz detachment, we used the six ZHe ages from the northern Boz Dağ flank because, in contrast to the nearly invariant AHe ages, they show a decrease in age in the down-dip direction of the detachment fault (i.e. toward the NNE). Using the distance between the samples in the tectonic transport direction, we derived a slip rate of 4.3 (+3.0/−1.2) mm a^{-1} ($R^2 = 0.75$; $p = 0.012$) for the time interval between *c.* 4 and *c.* 2 Ma by least-squares regression of the six data points (Fig. 5). The significance of the correlation coefficient was tested using *t*-statistics with a significance level of 0.05.

Exhumation history of the Boz Dağ block

Using the slip rate of *c.* 4.3 mm a^{-1} derived above, a vertical exhumation rate can be calculated for the rocks in the footwall of the Gediz detachment under the assumption that the present-day dip of 15° of the detachment represents the fault dip between *c.* 4 and 2 Ma. The resulting vertical exhumation rate is *c.* 1.1 km Ma^{-1}, which is a minimum estimate as the fault may have been steeper in the past. For a 30°-dipping fault, for example, the vertical exhumation rate would be 2.2 km Ma^{-1}; however, for reasons discussed below we consider a major rotation of the fault plane unlikely. The value of *c.* 1.1 km Ma^{-1} derived from the ZHe age–distance correlation can be compared with exhumation rates calculated from the cooling ages recorded by the various thermochronometers on the northern Boz Dağ flank under the assumption of a constant geothermal gradient (Fig. 6). The calculation of exhumation rates is performed using the closure temperatures mentioned above (AHe: 70 °C; AFT: 110 °C; ZHe: 180 °C; ZFT: 240 °C), a mean annual surface temperature of 10 °C for the Menderes Massif and a geothermal gradient of 40 °C km^{-1} estimated from the high average surface heat flow of *c.* 110 mW m^{-2} in the Menderes Massif (Ilkışık 1995) and heat flow models for the continental crust (Chapman & Furlong 1992). The resulting exhumation rates derived from AHe ages (1.7–2.5 Ma) and AFT ages (2.3 and 2.6 Ma) on the northern Boz Dağ flank are in the range of 0.6–0.9 and 1.0–1.1 km Ma^{-1}, respectively. In contrast, our ZHe ages (2.0–3.9 Ma) indicate higher exhumation rates between 1.1 and 2.2 km Ma^{-1} (Figs 4 and 6). The exhumation rate derived from the single ZFT age (6.4 Ma; sample 10JTB02) is *c.* 0.9 km Ma^{-1}. A similar exhumation rate of *c.* 1.1 km Ma^{-1} is indicated by a published ZFT cooling age of 5.2 Ma (Figs 4 and 6; Gessner *et al.* 2001*b*; sample T70).

Altogether, the data indicate that cooling and exhumation of rocks underneath the Gediz detachment apparently started to accelerate between *c.* 6 and 4 Ma and returned to lower rates after *c.* 2 Ma. For the time interval between *c.* 4 and 2 Ma, the exhumation rates derived from the conversion of the cooling rates are higher than the exhumation rate derived from the slip rate. This discrepancy may be explained by either a steeper fault dip or a temporarily higher fault slip rate. If we assume that the slip rate of *c.* 4 mm a^{-1} was constant, the peak exhumation rate of 2.2 km Ma^{-1} would imply a fault dip of *c.* 30°. However, as described above, the formation and preservation of the high-altitude sedimentary basins near the crest of the Boz Dağ block argues against a southward rotation of more than a few degrees (Süzen *et al.* 2006). Alternatively, the higher exhumation rate may be caused by a higher slip rate of *c.* 8–9 mm a^{-1} if we assume a constant dip of the fault plane of 15°. As some rotation is required to form the basins near the Boz Dağ crest line, our preferred interpretation to explain our data is a combination of minor fault plane rotation and a short-lived somewhat higher slip rate of the Gediz detachment during the time period between *c.* 4 and 2 Ma.

In contrast to the rocks in the footwall, our new age data from the augen gneiss klippen in the hanging wall of the Gediz detachment (Figs 4 and 7) indicate that these rocks cooled much earlier. Our ZHe and AFT ages indicate that the augen gneisses had already cooled below 110 °C by the middle Miocene. The good agreement between our AFT ages and the range of published AFT ages from the Küçük Menderes Graben (Gessner *et al.* 2001*b*; Ring *et al.* 2003) suggests that the klippen, which represent remnants of the Çine nappe farther south, experienced a similar cooling history to the gneisses of the Çine nappe exposed in the Küçük Menderes Graben (Figs 3a and 7). The final exhumation of the augen gneiss klippen occurred after the late Pliocene, as revealed by two AHe ages of 2.9 ± 0.8 Ma and 0.8 ± 0.2 Ma.

The cataclasite sample (11M8) taken from the fault plane of the Gediz detachment (i.e. in a structural position between the footwall and hanging wall) was apparently not thermally reset, because two of the three aliquots show ZHe ages of 17.4 ± 1.6 and 19.3 ± 1.6 Ma (Table 3). As these cooling ages are similar to the ZHe ages obtained from the augen gneiss klippen (Fig. 6a), we infer that these zircons are derived from hanging-wall rocks that were later incorporated into the brittle Gediz detachment. The ZHe age of the third aliquot (2.5 ± 0.2 Ma) agrees very well with the ZHe ages obtained from the three aliquots of sample 11M6, which is located close to 11M8 but in the fault footwall (Figs 3b and 4). Hence, the third aliquot of the cataclasite sample 11M8 is interpreted to represent material from the fault footwall. In contrast to the ZHe ages, the AHe age of 3.0 ± 1.8 Ma derived from a single apatite crystal in sample 11M8 (Table 2) is similar to AHe ages in both the fault footwall and hanging wall.

AHe and ZHe ages for samples near the peak and on the steep southern flank of Boz Dağ are higher than those on the northern flank and generally tend to increase with decreasing elevation toward the Küçük Menderes Graben (Fig. 6a). A similar trend can be observed in the published AFT data (Figs 4 and 6a), with the youngest AFT age (3.7 Ma) occurring at Boz Dağ peak and the oldest AFT age (22.2 Ma) occurring in the Küçük Menderes Graben (Gessner *et al.* 2001*b*; Ring *et al.* 2003). Using again a geothermal gradient of 40 °C km^{-1}, the combined age datasets can be converted to exhumation rates. Notably, the ages from all of the thermochronometers on the southern flank of Boz Dağ yield consistently lower exhumation rates than those on the northern flank (Fig. 6b). Including the sample from Boz Dağ peak, our AHe and ZHe data yield exhumation rates of 0.3–0.6 and 0.4–0.7 km Ma^{-1}, respectively. Exhumation rates derived from AFT data near Boz Dağ peak (Gessner *et al.* 2001*b*; Ring *et al.* 2003) also range from 0.3 to 0.7 km Ma^{-1}, whereas the rates are slightly lower (0.1–0.4 km Ma^{-1}) at the toe of the escarpment and in the Küçük Menderes Graben.

The combined thermochronological datasets of this study and previously published studies (Gessner *et al.* 2001*b*; Ring *et al.* 2003;

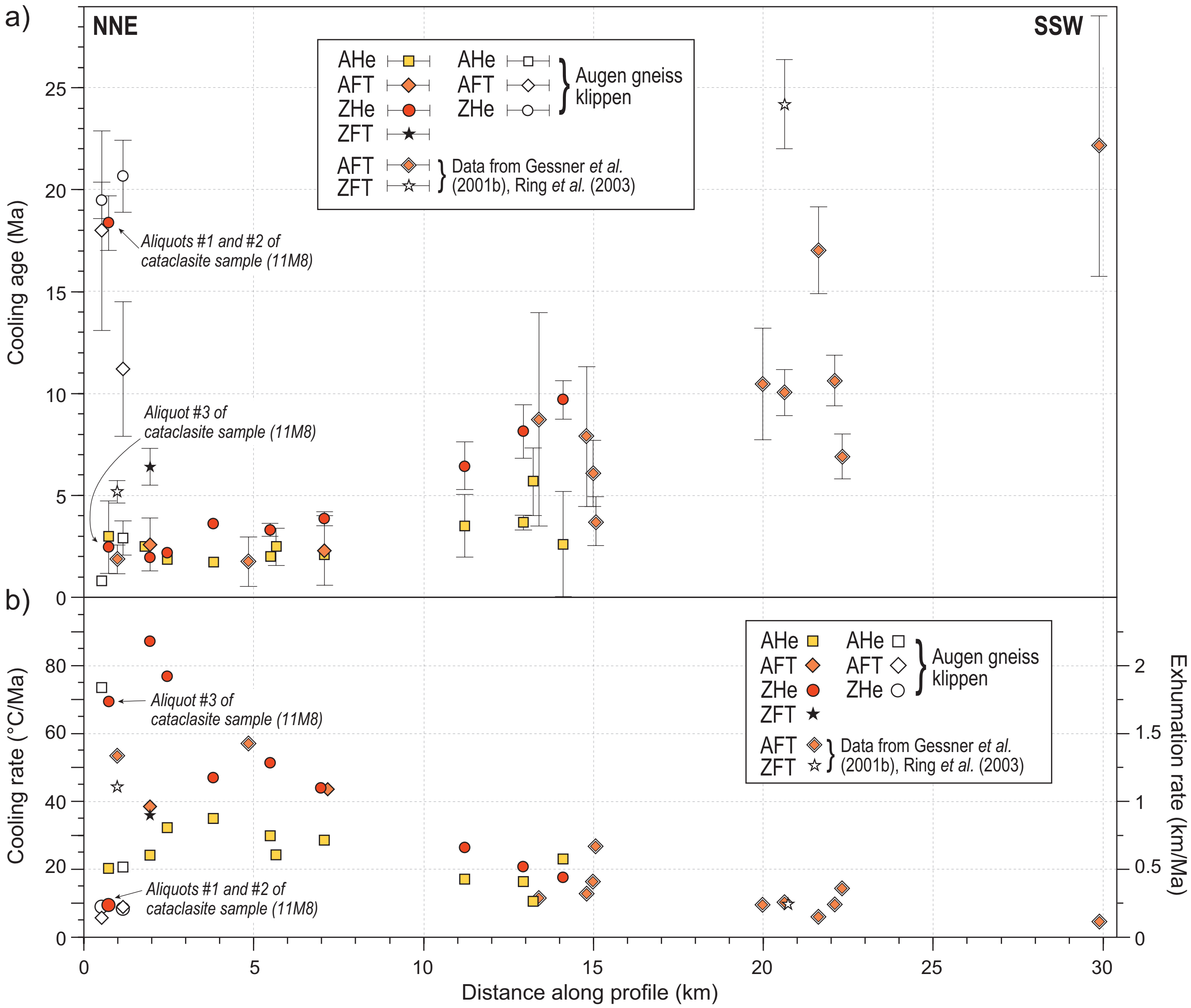

Fig. 6. (**a**) Cooling ages from this study, Gessner *et al.* (2001*b*) and Ring *et al.* (2003) plotted versus distance along a NNE–SSW profile (see Fig. 4 for location). Error bars are not shown if the error is smaller than the corresponding symbol size. Errors are 2 standard error for AHe and ZHe data and 2σ for AFT and ZFT data. (**b**) Cooling rates (left scale) and exhumation rates (right scale) plotted versus distance for the same datasets. All rates integrate over the time period between the corresponding cooling age and the present.

Fig. 6) suggest that the exhumation rate on the northern flank of the Boz Dağ block varied through time, and was higher in the Pliocene than before and afterwards. Such a pulse of tectonic activity was also inferred from the sedimentological record of the southern Gediz Graben, which indicates a major phase of extension during the latest Miocene(?)–Pliocene (Purvis & Robertson 2004, 2005).

Comparison of exhumation rates with short-term ^{10}Be erosion rates from Boz Dağ block

The long-term exhumation rates obtained from the thermochronological data for the southern Boz Dağ flank (100–700 mm ka^{-1}) have a similar magnitude to the ^{10}Be-derived erosion rates of *c.* 180–460 mm ka^{-1} for the catchments in this region (Fig. 4). If the erosion rates are representative of the last few million years, this implies that erosion played a significant if not dominant role in exhuming the rocks on the steep southern escarpment of Boz Dağ. The high rates of erosion can be explained as the combined effect of at least three factors. First, the amphibolite-facies two-mica schists and paragneisses that make up the Boz Dağ nappe (Dora *et al.* 1990, 2001; Hetzel *et al.* 1998) are highly susceptible to weathering and erosion. Second, the steep slopes along the escarpment (Fig. 2b; Table 5; Struffert 2012) promote fast erosion and allow the rapid removal of material from that region (see Palumbo *et al.* 2010). Third, the steeply southward-dipping foliation (Fig. 7), which is locally reactivated by normal faults (Fig. 2c), promotes erosion even further (see Rojay *et al.* 2005). Although the offsets on these normal faults are difficult to quantify, their cumulative fault displacement as well as the large-scale tilting of the Boz Dağ block appear to be responsible for the differential exhumation of the rock units between Boz Dağ peak and the Küçük Menderes Graben and can explain the observed inverse age–elevation relationship (Fig. 7).

Compared with the catchments in the south, the northern catchments erode at much lower rates of only 80–180 mm ka^{-1}, which

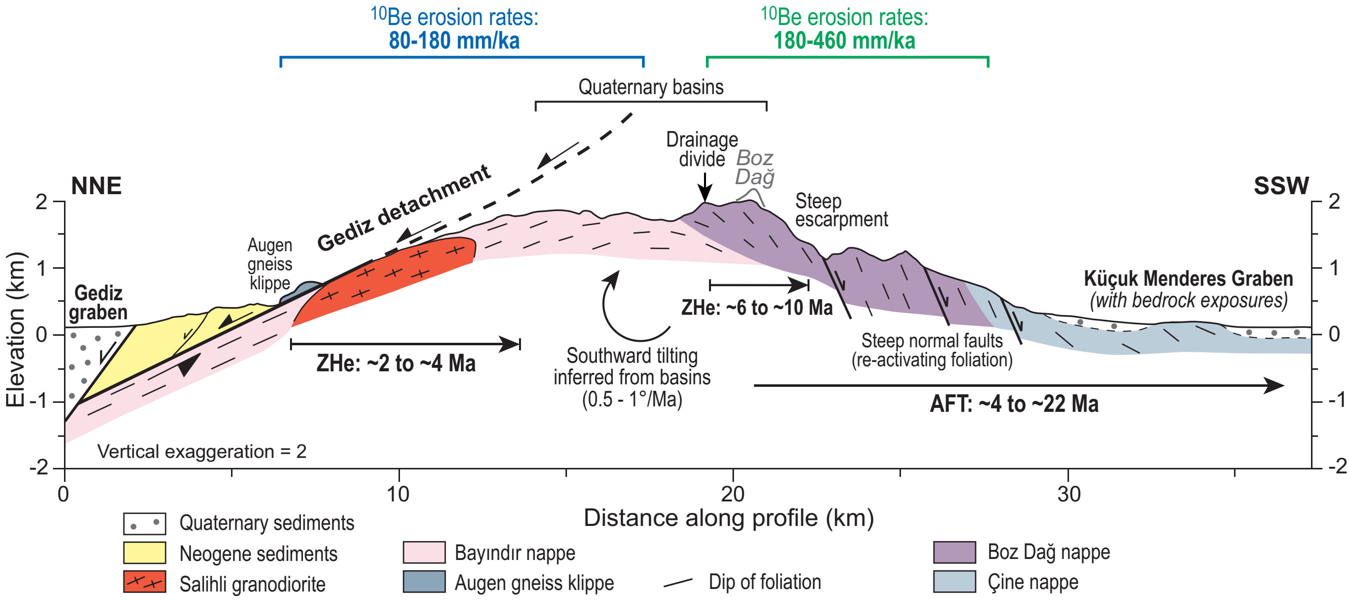

Fig. 7. Schematic profile across the Boz Dağ block summarizing the prominent tectonic and geomorphological features and the results from thermochronological (this study; Gessner *et al.* 2001*b*; Ring *et al.* 2003) and cosmogenic ^{10}Be data.

can be explained by the presence of quartz-rich lithologies that are less susceptible to erosion. In addition, the gently dipping mylonitic foliation and the lower hillslope angles do not favour rapid erosion (Table 5; Struffert 2012). Although local erosion rates on the northern slopes of Boz Dağ may have been temporarily higher during glacial periods, the resulting sediment would have been deposited in the small internally drained basins located north of this mountain (Fig. 3a). Hence, even if faster erosion had locally prevailed during cold periods, this would not affect our conclusion that north of Boz Dağ erosion is less important for rock exhumation than detachment faulting (Fig. 7). A north–south gradient in precipitation can be ruled out as a cause for the lower erosion rates on the northern flank because the mean annual precipitation rate is similar on both sides of the Boz Dağ block (Hijmans *et al.* 2005; Struffert 2012). Importantly, the ^{10}Be-derived erosion rates from the northern catchments are also significantly lower than the exhumation rates of *c.* 500–2000 mm ka^{-1} obtained from both the ZHe age–distance correlation and the conversion of cooling ages using a geothermal gradient of 40 °C km^{-1}. If the millennial catchment-wide erosion rates are representative of the last few million years, they support the notion that most exhumation on the northern Boz Dağ flank has occurred by tectonic denudation rather than erosion.

Implications for the tectonic evolution of the Menderes Massif

Our new thermochronological data indicate that crustal extension in the Boz Dağ region was accommodated by slip on the Gediz detachment, which was active as a low-angle normal fault until the end of the Pliocene or possibly the early Quaternary. Such a young age for detachment faulting is also consistent with the geomorphology of the northern flank of the Boz Dağ horst, where the cataclasites and mylonites of the spectacularly exposed Gediz detachment fault system exert the dominant control on the present-day landscape (Fig. 2a). Hence, the active normal fault along the southern margin of the Gediz Graben, which offsets the now inactive Gediz detachment (e.g. Bozkurt & Sözbilir 2004), is younger than commonly inferred; that is, Pleistocene rather than early Pliocene in age (e.g. Çemen *et al.* 2006). A transition from low-angle detachment to high-angle normal faulting between the late Pliocene and early Quaternary, when the modern Gediz Graben started to form, is also in accordance with the sedimentological and stratigraphic record of the Gediz supradetachment basin (e.g. Oner & Dilek 2011).

The trace of the modern graben-bounding fault is characterized by a distinct break-in-slope that extends all along the southern margin of the Gediz Graben and separates Pleistocene–Holocene alluvial fan sediments from uplifted Neogene sedimentary rocks in the footwall (Fig. 7; e.g. Paton 1992; Bozkurt Çiftçi & Bozkurt 2009). The 1969 M_s 6.5 Alaşehir earthquake, which was associated with a *c.* 30 km long surface break (Allen 1975), confirmed that this fault is seismically active. The main shock of the Alaşehir earthquake had a focal depth of 6 km and resulted from slip on a fault plane that on average dips 32° to the NNE (Eyidogan & Jackson 1985). Hence, a seismically active low-angle normal fault similar to the Gediz detachment appears to be present underneath the Gediz Graben and it is likely that this fault also caused the devastating AD 17 earthquake that destroyed 12 Roman cities between the Aegean coast and Alaşehir (Ambraseys 1971).

In the past, active slip on low-angle normal faults was often considered impossible because brittle faulting occurs on planes oriented at an angle of *c.* 30° to the maximum principal stress σ_1, which is vertical in extensional settings (Anderson 1951). However, an increasing number of geological, geophysical and/or space-geodetic studies in actively extending regions such as the Aegean (Rietbrock *et al.* 1996; Rigo *et al.* 1996; Laigle *et al.* 2000; Sorel 2000; Lecomte *et al.* 2010), the Apennines (Hreinsdóttir & Bennett 2009) and southern Tibet (Monigle *et al.* 2012) have shown that low-angle normal faults can indeed accumulate slip. A mechanical explanation for the apparent paradox of low-angle normal faulting was given by Melosh (1990) and Westaway (1999), who argued that a deforming lower crust with low viscosity may cause a significant rotation of the main principal stresses in the mid-crust. In this regard, it is noteworthy that regions with active low-angle normal faulting are generally characterized by magmatic activity and/or an elevated heat flow, which indicates the presence of a hot and weak lower crust.

In the northern and central Menderes Massif, widespread magmatic activity occurred since the Early Miocene and changed in character from calc-alkaline to alkaline in the Middle Miocene (e.g. Seyitoğlu *et al.* 1997). The age of the volcanic rocks generally decreases southward (e.g. from 20 to 4 Ma for ultrapotassic lamproitic rocks), and records an increasing contribution of melts derived from the asthenosphere with time (Prelević *et al.* 2012). The age and geochemical trends can be explained by an upwelling of the asthenosphere and a progressive thinning of the lithospheric mantle, which are presumably caused by the rollback of the Hellenic slab underneath the Aegean and western Turkey (e.g. Brun & Sokoutis 2010; Prelević *et al.* 2012). A southward retreat of the subducting slab appears to be consistent with the fact that the earliest phase of low-angle normal faulting took place on the Simav detachment in the northern Menderes Massif between *c.* 25 and 19 Ma (Thomson & Ring 2006). Subsequently, detachment faulting started in the central Menderes Massif where the syn-extensional Salihli and Turgutlu granodiories intruded the Gediz detachment fault system at *c.* 15 and *c.* 16 Ma (Glodny & Hetzel 2007). The enhanced Pliocene tectonic activity of the Gediz detachment may be related to a phase of lithospheric thinning beneath the Kula region (*c.* 20 km north of the eastern Gediz Graben), which ultimately resulted in the extrusion of alkali basalts of Quaternary age (Richardson-Bunbury 1996; Tokçaer *et al.* 2005). Hence, the Kula region is presumably underlain by a lower crust with a strongly reduced viscosity (Westaway *et al.* 2004). A hot and weak lower crust may also be present beneath adjacent areas including the Boz Dağ region, as indicated by high surface heat flow values of >100 mW m^{-2} (Ilkışık 1995) and low P-wave velocities as well as the observation that the depth of earthquake hypocentres generally does not exceed *c.* 10 km (Akyol *et al.* 2006). In concert, slab rollback and upwelling of the asthenosphere beneath western Turkey may hence have created favourable conditions for active low-angle normal faulting in the central Menderes Massif.

Conclusions

Based on new thermochronological data and ^{10}Be-derived erosion rates, we have provided constraints on rock exhumation, normal faulting and landscape development in the central Menderes Massif. In particular, our data allow us to derive constraints on the relative importance of exhumation and erosion in the Boz Dağ region. On the northern flank, tectonic denudation owing to low-angle detachment faulting predominates over erosion, whereas long-term exhumation rates and short-term ^{10}Be-based erosion rates are similar on the southern flank. Our ZHe data from the footwall of the Gediz detachment yielded a slip rate of 4.3 (+3.0/−1.2) mm a^{-1} for the late Pliocene to early Pleistocene. As a significant rotation of the Gediz detachment in the past is unlikely and an active seismogenic low-angle fault is present beneath the modern Gediz Graben, the central Menderes Massif provides another example of a region with low-angle normal faulting. As in other regions, this process may be promoted by slab rollback, asthenospheric upwelling and subsequent lithospheric thinning.

We thank three anonymous reviewers for their constructive comments. We thank C. Wenske (Universität Hannover) for help with the preparation of the low-temperature thermochronology samples, A. Niehus (Universität Münster) for help in the laboratory during preparation of the ^{10}Be samples, V. Rapelius (Universität Münster) for ICP analyses, and P. Kubik (ETH Zurich) for the AMS analyses. Some of the maps and diagrams shown in the figures were created with the Generic Mapping Tools (GMT) by Wessel & Smith (1998). Preparation of low-temperature thermochronology samples, fission-track analyses and He analyses were funded by start-up funds provided to A.H. by the Leibniz-Universität Hannover. Cosmogenic nuclide sample preparation and AMS analyses were funded by a pilot study grant provided to R.H. by the Faculty of Geosciences at the Universität Münster. Costs for fieldwork in Turkey in 2010 and 2011 were shared between the working groups in Hannover and Münster.

References

Aktug, B., Nocquet, J.M., *et al.* 2009. Deformation of western Turkey from a combination of permanent and campaign GPS data: Limits to block-like behavior. *Journal of Geophysical Research*, **114**, B10404, http://dx.doi.org/10.1029/2008JB006000.

Akyol, N., Zhu, L., Mitchell, B.J., Sözbilir, H. & Kekovali, K. 2006. Crustal structure and local seismicity in western Anatolia. *Geophysical Journal International*, **166**, 1259–1269.

Allen, C.R. 1975. Geological criteria for evaluating seismicity. *Geological Society of America Bulletin*, **86**, 1041–1057.

Ambraseys, N.N. 1971. Value of historical records of earthquakes. *Nature*, **232**, 375–379.

Anderson, E.M. 1951. *The Dynamics of Faulting*. Oliver & Boyd, London.

Armstrong, P.A., Ehlers, T.A., Chapman, D.S., Farley, K.A. & Kamp, P.J.J. 2003. Exhumation of the central Wasatch Mountains, Utah: 1. Patterns and timing of exhumation deduced from low-temperature thermochronology data. *Journal of Geophysical Research*, **108**, 2172, http://dx.doi.org/10.1029/2001JB001708.

Armstrong, P.A., Taylor, A.R. & Ehlers, T.A. 2004. Is the Wasatch fault footwall (Utah, United States) segmented over million-year time scales? *Geology*, **32**, 385–388.

Balco, G., Stone, J.O., Lifton, N.A. & Dunai, T.J. 2008. A complete and easily accessible means of calculating surface exposure ages or erosion rates from ^{10}Be and ^{26}Al measurements. *Quaternary Geochronology*, **3**, 174–195.

Benedetti, L., Finkel, R., *et al.* 2002. Post-glacial slip history of the Sparta fault (Greece) determined by ^{36}Cl cosmogenic dating: Evidence for non-periodic earthquakes. *Geophysical Research Letters*, **29**, http://dx.doi.org/10.1029/2001GL014510.

Bierman, P. & Steig, E.J. 1996. Estimating rates of denudation using cosmogenic isotope abundances in sediment. *Earth Surface Processes and Landforms*, **21**, 125–139.

Bozkurt, E. & Park, G. 1994. Southern Menderes Massif—an incipient metamorphic core complex in western Anatolia, Turkey. *Journal of the Geological Society, London*, **151**, 213–216.

Bozkurt, E. & Sözbilir, H. 2004. Tectonic evolution of the Gediz Graben: Field evidence for an episodic, two-stage extension in western Turkey. *Geological Magazine*, **141**, 63–79.

Bozkurt, E., Winchester, J.A., Ruffet, G. & Rojay, B. 2008. Age and chemistry of Miocene volcanic rocks from the Kiraz Basin of the Kücük Menderes Graben: its significance for the extensional tectonics of southwestern Anatolia, Turkey. *Geodinamica Acta*, **21**, 239–257.

Bozkurt Çiftçi, N. & Bozkurt, E. 2009. Pattern of normal faulting in the Gediz Graben, SW Turkey. *Tectonophysics*, **473**, 234–260.

Brady, R.J. 2002. Very high slip rates on continental extensional faults: new evidence from (U–Th)/He thermochronometry of the Buckskin Mountains, Arizona. *Earth and Planetary Science Letters*, **197**, 95–104.

Brichau, S., Ring, U., Ketcham, R.A., Carter, A., Stockli, D. & Brunel, M. 2006. Constraining the long-term evolution of the slip rate for a major extensional fault system in the central Aegean, Greece, using thermochronology. *Earth and Planetary Science Letters*, **241**, 293–306.

Brichau, S., Ring, U., Carter, A., Bolhar, R., Monié, P., Stockli, D. & Brunel, M. 2008. Timing, slip rate, displacement and cooling history of the Mykonos detachment footwall, Cyclades, Greece, and implications for the opening of the Aegean Sea basin. *Journal of the Geological Society, London*, **165**, 263–277.

Brun, J.-P. & Sokoutis, D. 2010. 45 m.y. of Aegean crust and mantle flow driven by trench retreat. *Geology*, **38**, 815–818.

Burtner, R., Nigrini, A. & Donelick, R.A. 1994. Thermochronology of Lower Cretaceous source rocks in the Idaho–Wyoming Thrust belt. *AAPG Bulletin*, **78**, 1613–1636.

Candan, O., Dora, O.Ö., Oberhänsli, R., Cetinkaplan, M., Partzsch, J.H., Warkus, F.C. & Dürr, S. 2001. Pan-African high-pressure metamorphism in the Precambrian basement of the Menderes Massif, western Anatolia, Turkey. *International Journal of Earth Sciences*, **89**, 793–811.

Çemen, I., Catlos, E.J., Gogus, O. & Ozerdem, C. 2006. Post-collisional extensional tectonics and exhumation of the Menderes massif in the western Anatolia Extended Terrane, Turkey. *In*: Dilek, Y. & Pavlides, S. (eds) *Post-collisional Tectonics and Magmatism in the Eastern Mediterranean Region*. Geological Society of America, Special Papers, **409**, 353–379.

Chapman, D.S. & Furlong, K.P. 1992. Thermal state of the continental lower crust. *In*: Fountain, D.M., Arculus, R. & Kay, R.W. (eds) *Continental Lower Crust*. Elsevier, Amsterdam, 179–199.

Chmeleff, J., Von Blanckenburg, F., Kossert, K. & Jakob, D. 2010. Determination of the ^{10}Be half-life by multicollector ICP-MS and liquid scintillation counting. *Nuclear Instruments and Methods in Physics Research B*, **268**, 192–199.

Crittenden, M.D., Coney, P.J. & Davis, G.H. 1980. *Cordilleran Metamorphic Core Complexes*. Geological Society of America, Memoirs, **153**.

Densmore, A.L., Hetzel, R., Ivy-Ochs, S., Krugh, W.C., Dawers, N. & Kubik, P.W. 2009. Spatial variations in catchment-averaged denudation rates from normal fault footwalls. *Geology*, **37**, 1139–1142.

Desilets, D., Zreda, M. & Prabu, T. 2006. Extended scaling factors for *in situ* cosmogenic nuclides: new measurements at low latitude. *Earth and Planetary Science Letters*, **246**, 265–276.

Dewey, J.F. 1988. Extensional collapse of orogens. *Tectonics*, **7**, 1123–1139.

Dora, O.Ö., Kun, N. & Candan, O. 1990. Metamorphic history and geotectonic evolution of the Menderes Massif. *In*: Savascin, M.Y. & Eronat, A.H. (eds) *International Earth Sciences Congress on Aegean Regions, Proceedings*. IESCA, 102–115.

Dora, O.Ö., Candan, O., Kaya, O., Koralay, E. & Dürr, S. 2001. Revision of 'Leptite-gneisses' in the Menderes Massif: A supracrustal metasedimentary origin. *International Journal of Earth Sciences*, **89**, 836–851.

Dunai, T.J. 2001. Influence of secular variation of the geomagnetic field on production rates of *in situ* produced cosmogenic nuclides. *Earth and Planetary Science Letters*, **193**, 197–212.

Ehlers, T.A. & Farley, K.A. 2003. Apatite (U–Th)/He thermochronometry: methods and applications to problems in tectonics and surface processes. *Earth and Planetary Science Letters*, **206**, 1–14.

Ehlers, T.A., Willett, S.D., Armstrong, P.A. & Chapman, D.S. 2003. Exhumation of the central Wasatch Mountains, Utah: 2. Thermokinematic model of exhumation, erosion, and thermochronometer interpretation. *Journal of Geophysical Research*, **108**, 2173, http://dx.doi.org/10.1029/2001JB001723.

Emre, T. 1996. The tectonic evolution of the Gediz graben. *Geological Bulletin of Turkey*, **39**, 1–18.

Emre, T. & Sözbilir, H. 2007. Tectonic evolution of the Kiraz Basin, Küçük Menderes Graben: evidence for compression/uplift-related basin formation overprinted by extensional tectonics in West Anatolia. *Turkish Journal of Earth Sciences*, **16**, 441–470.

England, P. & Molnar, P. 1990. Surface uplift, uplift of rocks, and exhumation of rocks. *Geology*, **18**, 1173–1177.

Eyidogan, H. & Jackson, J. 1985. A seismological study of normal faulting in the Demirci, Alaşehir and Gediz earthquakes of 1969–70 in western Turkey: Implications for the nature and geometry of deformation in the continental crust. *Geophysical Journal of the Royal Astronomical Society*, **81**, 569–607.

Farley, K.A. 2000. Helium diffusion from apatite: General behavior as illustrated by Durango fluorapatite. *Journal of Geophysical Research*, **105**, 2903–2914.

Farley, K.A., Wolf, R.A. & Silver, L.T. 1996. The effects of long alpha-stopping distances on (U–Th)/He ages. *Geochimica et Cosmochimica Acta*, **60**, 4223–4229.

Fitzgerald, P.G., Fryxell, J.E. & Wernicke, B.P. 1991. Miocene crustal extension and uplift in southeastern Nevada: Constraints from apatite fission track analysis. *Geology*, **19**, 1013–1016.

Flowers, R.M., Shuster, D.L. & Farley, K.A. 2007. Radiation damage control on apatite (U–Th)/He dates from the Grand Canyon region, Colorado Plateau. *Geology*, **35**, 447–450.

Foster, D.A. & John, B.E. 1999. Quantifying tectonic exhumation in an extensional orogen with thermochronology: Examples from the southern Basin and Range Province. *In*: Ring, U., Brandon, M.T., Lister, G.S. & Willett, S.D. (eds) *Exhumation Processes: Normal Faulting, Ductile Flow, and Erosion*. Geological Society, London, Special Publications, **154**, 343–364.

Frisch, W., Dunkl, I. & Kuhlemann, J. 2000. Post-collisional large-scale extension in the Eastern Alps. *Tectonophysics*, **327**, 239–265.

Fügenschuh, B., Seward, D. & Mancktelow, N. 1997. Exhumation in a convergent orogen: The western Tauern window. *Terra Nova*, **9**, 213–217.

Gallagher, K., Brown, R. & Johnson, C. 1998. Fission track analysis and its applications to geological problems. *Annual Review of Earth and Planetary Sciences*, **26**, 519–572.

Gautier, P. & Brun, J.P. 1994. Ductile crust exhumation and extensional detachments in the central Aegean (Cyclades and Evvia islands). *Geodinamica Acta*, **7**, 57–85.

Gessner, K., Piazolo, S., Güngör, T., Ring, U., Kröner, A. & Passchier, C.W. 2001*a*. Tectonic significance of deformation patterns in granitoid rocks of the Menderes nappes, Anatolide belt, southwest Turkey. *International Journal of Earth Sciences*, **89**, 766–780.

Gessner, K., Ring, U., Johnson, C., Hetzel, R., Passchier, C.W. & Güngör, T. 2001*b*. An active bivergent rolling-hinge detachment system: Central Menderes metamorphic core complex in western Turkey. *Geology*, **29**, 611–614.

Gessner, K., Gallardo, L.A., Markwitz, V., Ring, U. & Thomson, S.N. 2013. What caused the denudation of the Menderes Massif: Review of crustal evolution, lithosphere structure, and dynamic topography in southwest Turkey. *Gondwana Research*, **24**, 243–274, doi:10.1016/j.gr.2013.01.005.

Gleadow, A.J.W. & Duddy, I.R. 1981. A natural long-term track annealing experiment for apatite. *Nuclear Tracks*, **5**, 169–174.

Glodny, J. & Hetzel, R. 2007. Precise U–Pb ages of syn-extensional Miocene intrusions in the central Menderes Massif, western Turkey. *Geological Magazine*, **144**, 235–246.

Goethals, M.M., Hetzel, R., *et al.* 2009. An improved experimental determination of cosmogenic ^{10}Be/^{21}Ne and ^{26}Al/^{21}Ne production ratios in quartz. *Earth and Planetary Science Letters*, **284**, 187–198.

Granger, D.E., Kirchner, J.W. & Finkel, R. 1996. Spatially averaged long-term erosion rates measured from *in situ* produced cosmogenic nuclides in alluvial sediment. *Journal of Geology*, **104**, 249–257.

Grasemann, B., Schneider, D.A., Stockli, D.F. & Iglseder, C. 2012. Miocene bivergent crustal extension in the Cyclades (Greece). *Lithosphere*, **4**, 23–39.

Herman, F., Braun, J., Senden, T.J. & Dunlap, W.J. 2007. (U–Th)/He thermochronometry: mapping 3D geometry using micro-X-ray tomography and solving the associated production–diffusion equation. *Chemical Geology*, **242**, 126–136.

Hetzel, R., Ring, U., Akal, C. & Troesch, M. 1995*a*. Miocene NNE-directed extensional unroofing in the Menderes Massif, southwestern Turkey. *Journal of the Geological Society, London*, **152**, 639–654.

Hetzel, R., Passchier, C.W., Ring, U. & Dora, O.Ö. 1995*b*. Bivergent extension in orogenic belts: The Menderes Massif (southwestern Turkey). *Geology*, **23**, 455–458.

Hetzel, R., Romer, R.L., Candan, O. & Passchier, C.W. 1998. Geology of the Bozdag area, central Menderes massif, SW Turkey: Pan-African basement and Alpine deformation. *Geologische Rundschau*, **87**, 394–406.

Hijmans, R.J., Cameron, S.E., Parra, J.L., Jones, P.G. & Jarvis, A. 2005. Very high resolution interpolated climate surface for global land areas. *International Journal of Climatology*, **25**, 1965–1978.

Hourigan, J.K., Reiners, P.W. & Brandon, M.T. 2005. U–Th zonation-dependent alpha-ejection in (U–Th)/He chronometry. *Geochimica et Cosmochimica Acta*, **69**, 3349–3365, http://dx.doi.org/10.1016/j.gca.2005.01.024.

Hreinsdóttir, S. & Bennett, R.A. 2009. Active aseismic creep on the Alto Tiberina low-angle normal fault, Italy. *Geology*, **37**, 683–686.

Hughes, P.D., Gibbard, P.L. & Woodward, J.C. 2006. Middle Pleistocene glacier behaviour in the Mediterranean: sedimentological evidence from the Pindus Mountains, Greece. *Journal of the Geological Society, London*, **163**, 857–867.

Hughes, P.D., Woodward, J.C., van Calsteren, P.C. & Thomas, L.E. 2011. The glacial history of the Dinaric Alps, Montenegro. *Quaternary Science Reviews*, **30**, 3393–3412.

Hurford, A.J. & Green, P.F. 1983. The zeta age calibration of fission-track dating. *Chemical Geology*, **1**, 285–317.

Ilkişik, O.M. 1995. Regional heat flow in western Anatolia using silica temperature estimates from thermal springs. *Tectonophysics*, **244**, 175–184.

Işik, V., Seyitoğlu, G. & Çemen, I. 2003. Ductile–brittle transition along the Alaşehir detachment fault and its structural relationship with the Simav detachment fault, Menderes massif, western Turkey. *Tectonophysics*, **374**, 1–18.

Jackson, J. 1994. Active tectonics of the Aegean Region. *Annual Review of Earth and Planetary Sciences*, **22**, 239–271.

John, B.E. & Howard, K.A. 1995. Rapid extension recorded by cooling-age patterns and brittle deformation, Naxos, Greece. *Journal of Geophysical Research*, **100**, 9969–9979.

Ketcham, R.A. 1996. Thermal models of core-complex evolution in Arizona and New Guinea: implications for ancient cooling paths and present-day heatflow. *Tectonics*, **15**, 933–951.

Kohl, C.P. & Nishiizumi, K. 1992. Chemical isolation of quartz for measurement of *in-situ* produced cosmogenic nuclides. *Geochimica et Cosmochimica Acta*, **56**, 3583–3587.

Korschinek, G., Bergmaier, A., *et al.* 2010. A new value for the half-life of ^{10}Be by Heavy-Ion Elastic Recoil Detection and liquid scintillation counting. *Nuclear Instruments and Methods in Physics Research B*, **268**, 187–191.

Kubik, P.W. & Christl, M. 2010. ^{10}Be and ^{26}Al measurements at the Zurich 6 MV Tandem AMS facility. *Nuclear Instruments and Methods in Physics Research B*, **268**, 880–883.

Laigle, M., Hirn, A., Sachpazi, M. & Roussos, N. 2000. North Aegean crustal deformation: an active fault imaged to 10 km depth by reflection seismic data. *Geology*, **28**, 71–74.

Lal, D. 1991. Cosmic ray labeling of erosion surfaces: *In situ* nuclide production rates and erosion models. *Earth and Planetary Science Letters*, **104**, 424–439.

Lecomte, E., Jolivet, L., Lacombe, O., Denèle, Y., Labrousse, L. & Le Pourhiet, L. 2010. Geometry and kinematics of Mykonos detachment, Cyclades, Greece: Evidence for slip at shallow dip. *Tectonics*, **29**, TC5012, http://dx.doi.org/10.1029/2009TC002564.

Lee, J. & Lister, G.S. 1992. Late Miocene ductile extension and detachment faulting, Mykonos, Greece. *Geology*, **20**, 121–124.

Lifton, N.A., Bieber, J.W., Clem, J.M., Duldig, M.L., Evenson, P., Humble, J.E. & Pyle, R. 2005. Addressing solar modulation and long-term uncertainties in scaling secondary cosmic rays for *in situ* cosmogenic nuclide applications. *Earth and Planetary Science Letters*, **239**, 140–161.

Lippolt, H.J., Leitz, M., Wernicke, R.S. & Hagerdon, B. 1994. (Uranium + thorium)/helium dating of apatite: experience with samples from different geochemical environments. *Chemical Geology*, **112**, 179–191.

Lister, G.S. & Davis, G.A. 1989. The origin of metamorphic core complexes and detachment faults formed during Tertiary continental extension in the northern Colorado River region, U.S.A. *Journal of Structural Geology*, **11**, 65–94.

Mancktelow, N.S. 1992. Neogene lateral extension during convergence in the Central Alps: Evidence from interrelated faulting and backfolding around the Simplonpass (Switzerland). *Tectonophysics*, **215**, 295–317.

Melosh, H.J. 1990. Mechanical basis for low-angle normal faulting in the Basin and Range province. *Nature*, **343**, 331–335.

Monigle, P.W., Nabelek, J., Braunmiller, J. & Carpenter, N.S. 2012. Evidence for low-angle normal faulting in the Pumqu–Xianza Rift, Tibet. *Geophysical Journal International*, **190**, 1335–1340.

Naeser, C.W. 1978. *Fission Track Dating*. US Geological Survey Open-File Report, **76–190**.

Nishiizumi, K., Imamura, M., Caffee, M.W., Southon, J.R., Finkel, R.C. & McAninch, J. 2007. Absolute calibration of ^{10}Be AMS standards. *Nuclear Instruments and Methods in Physics Research B*, **258**, 403–413.

Oberhänsli, R., Candan, O., Dora, O.Ö. & Dürr, S.H. 1997. Eclogites within the Menderes Massif western Turkey. *Lithos*, **41**, 135–150.

Oner, Z. & Dilek, Y. 2011. Supradetachment basin evolution during continental extension: the Aegean province of western Anatolia, Turkey. *Geological Society of America Bulletin*, **123**, 2115–2141.

Palumbo, L., Hetzel, R., Tao, M. & Li, X. 2010. Topographic and lithologic control on catchment-wide denudation rates derived from cosmogenic ^{10}Be in two mountain ranges at the margin of NE Tibet. *Geomorphology*, **117**, 130–142.

Paton, S. 1992. Active normal faulting, drainage patterns and sedimentation in southwestern Turkey. *Journal of the Geological Society, London*, **149**, 1031–1044.

Prelević, D., Akal, C., Foley, S.F., Romer, R.L., Stracke, A. & van den Bogaard, P. 2012. Ultrapotassic mafic rocks as geochemical proxies for post-collisional dynamics of orogenic lithospheric mantle: The case of southwestern Anatolia, Turkey. *Journal of Petrology*, **53**, 1019–1055.

Purvis, M. & Robertson, A. 2004. A pulsed extension model for the Neogene–Recent E–W-trending Alaşehir Graben and the NE–SW-trending Selendi and Gördes Basins, western Turkey. *Tectonophysics*, **391**, 171–201.

Purvis, M. & Robertson, A. 2005. Sedimentation of the Neogene–Recent Alaşehir (Gediz) continental graben system used to test alternative tectonic models for western (Aegean) Turkey. *Sedimentary Geology*, **173**, 373–408.

Rahn, M.K., Brandon, M.T., Batt, G.E. & Garver, J.I. 2004. A zero-damage model for fission-track annealing in zircon. *American Mineralogist*, **89**, 473–484.

Ratschbacher, L., Frisch, W., Neubauer, F., Schmid, S.M. & Neugebauer, J. 1989. Extension in compressional orogenic belts: The eastern Alps. *Geology*, **17**, 404–407.

Reiners, P.W. & Brandon, M.T. 2006. Using thermochronology to understand orogenic erosion. *Annual Review of Earth and Planetary Sciences*, **34**, 419–466.

Reiners, P.W. & Ehlers, T.A. (eds). 2005. *Low-temperature Thermochronology: Techniques, Interpretations, and Applications*. Mineralogical Society of America and Geochemical Society, Reviews in Mineralogy and Geochemistry, **58**.

Reiners, P.W., Spell, T.I., Nicolescu, S. & Zanetti, K. 2004. Zircon (U–Th)/He thermochronometry: He diffusion and comparisons with ^{40}Ar/^{39}Ar dating. *Geochimica et Cosmochimica Acta*, **68**, 1857–1887.

Richardson-Bunbury, J.M. 1996. The Kula volcanic field, western Turkey; The development of a Holocene alkali basalt province and the adjacent normal-faulting graben. *Geological Magazine*, **133**, 275–283.

Rietbrock, A., Tiberi, C., Scherbaum, F. & Lyon-Caen, H. 1996. Seismic slip on a low angle normal fault in the Gulf of Corinth: Evidence from high-resolution cluster analysis of micro-earthquakes. *Geophysical Research Letters*, **23**, 1817–1820.

Rigo, A., Lyon-Caen, H., *et al.* 1996. A microseismic study in the western part of the Gulf of Corinth (Greece): Implications for large-scale normal faulting mechanisms. *Geophysical Journal International*, **126**, 663–688.

Ring, U., Brandon, M.T., Lister, G.S. & Willett, S.D. 1999. Exhumation processes. *In*: Ring, U., Brandon, M.T., Lister, G.S. & Willett, S.D. (eds) *Exhumation Processes: Normal Faulting, Ductile Flow, and Erosion*. Geological Society, London, Special Publications, **154**, 1–27.

Ring, U., Layer, P.W. & Reischmann, T. 2001. Miocene high-pressure metamorphism in the Cyclades and Crete, Aegean Sea, Greece: Evidence for large-magnitude displacement on the Cretan detachment. *Geology*, **29**, 395–398.

Ring, U., Johnson, C., Hetzel, R. & Gessner, K. 2003. Tectonic denudation of a late Cretaceous–Tertiary collisional belt: Regionally symmetric cooling patterns and their relation to extensional faults in the Anatolide belt of western Turkey. *Geological Magazine*, **140**, 421–441.

Rojay, B., Toprak, V., Demirci, C. & Süzen, L. 2005. Plio-Quaternary evolution of the Küçük Menderes Graben, Southwestern Anatolia, Turkey. *Geodinamica Acta*, **18**, 317–331.

Rutherford, E. 1905. Present problems in radioactivity. *Popular Science*, **67**, 1–34.

Sarikaya, M.A., Zreda, M., Çiner, A. & Zweck, C. 2008. Cold and wet Last Glacial Maximum on Mount Sandıras, SW Turkey, inferred from cosmogenic dating and glacier modeling. *Quaternary Science Reviews*, **27**, 769–780.

Sen, S. & Seyitoğlu, G. 2009. Magnetostratigraphy of early–middle Miocene deposits from east–west trending Alasehir and Büyük Menderes grabens in western Turkey, and its tectonic implications. *In*: van Hinsbergen, D.J.J., Edwards, M.A. & Govers, R. (eds) *Collision and Collapse at the Africa–Arabia–Eurasia Subduction Zone*. Geological Society, London, Special Publications, **311**, 321–342.

Seyitoğlu, G. & Scott, B.C. 1991. Late Cenozoic crustal extension and basin formation in west Turkey. *Geological Magazine*, **128**, 155–166.

Seyitoğlu, G., Anderson, D., Nowell, G. & Scott, B. 1997. The evolution from Miocene potassic to Quaternary sodic magmatism in western Turkey: Implications for enrichment processes in the lithospheric mantle. *Journal of Volcanology and Geothermal Research*, **76**, 127–147.

Seyitoğlu, G., Tekeli, O., Çemen, I., Sen, S. & Isik, V. 2002. The role of the flexural rotation/rolling hinge model on the tectonic evolution of the Alasehir graben, western Turkey. *Geological Magazine*, **139**, 15–26.

Sorel, D. 2000. A Pleistocene and still-active detachment fault and the origin of the Corinth–Patras rift, Greece. *Geology*, **28**, 83–86.

Stock, G.M., Frankel, K.L., Ehlers, T.A., Schaller, M., Briggs, S.M. & Finkel, R.C. 2009. Spatial and temporal variations in denudation of the Wasatch Mountains, Utah, USA. *Lithosphere*, **1**, 34–40.

Stockli, D.F. 2005. Application of low-temperature thermochronometry to extensional tectonic settings. *In*: Reiners, P.W. & Ehlers, T.A. (eds) *Low-temperature Thermochronology: Techniques, Interpretations, and Applications*. Mineralogical Society of America and Geochemical Society, Reviews in Mineralogy and Geochemistry, **58**, 411–466.

Stockli, D.F., Surpless, B.E. & Dumitru, T.A. 2002. Thermochronological constraints on the timing and magnitude of Miocene and Pliocene extension in the central Wassuk Range, western Nevada. *Tectonics*, **21**, http://dx.doi.org/10.1029/2001TC001295.

Stone, J.O. 2000. Air pressure and cosmogenic isotope production. *Journal of Geophysical Research*, **105**, 23753–23759.

Struffert, A. 2012. *^{10}Be-derived denudation rates in the central Menderes Massif, southwestern Turkey*. MSc thesis, Westfälische Wilhelms-Universität Münster.

Süzen, M.L., Toprak, V. & Rojay, B. 2006. High-altitude Plio-Quaternary fluvial deposits and their implication on the tilt of a horst, western Anatolia, Turkey. *Geomorphology*, **74**, 80–99.

Thomson, S.N. & Ring, U. 2006. Thermochronologic evaluation of postcollision extension in the Anatolide orogen, western Turkey. *Tectonics*, **25**, TC3005, http://dx.doi.org/10.1029/2005TC001833.

Tokçaer, M., Agostini, S. & Savaşçin, M.Y. 2005. Geotectonic setting and origin of the youngest Kula volcanics (western Anatolia), with a new emplacement model. *Turkish Journal of Earth Sciences*, **14**, 145–166.

von Blanckenburg, F. 2006. The control mechanisms of erosion and weathering at basin scale from cosmogenic nuclides in river sediment. *Earth and Planetary Science Letters*, **242**, 224–239.

Wagner, G.A. & Van den Haute, P. 1992. Fission-track Dating. Kluwer, Dordrecht.

Wernicke, B., Axen, G.J. & Snow, J.K. 1988. Basin and Range extensional tectonics at the latitude of Las Vegas, Nevada. *Geological Society of America Bulletin*, **100**, 1738–1757.

Wessel, P. & Smith, W.H.F. 1998. New, improved version of the Generic Mapping Tools released. *EOS Transactions American Geophysical Union*, **79**, 579.

Westaway, R. 1999. The mechanical feasibility of low-angle normal faulting. *Tectonophysics*, **308**, 407–443.

Westaway, R., Pringle, M., Yurtmen, S., Demir, T., Bridgland, D., Rowbotham, G. & Maddy, D. 2004. Pliocene and Quaternary regional uplift in western Turkey: the Gediz River terrace staircase and the volcanism at Kula. *Tectonophysics*, **391**, 121–169.

Wolf, R.A., Farley, K.A. & Silver, L.T. 1996. Helium diffusion and low temperature thermochronology of apatite. *Geochimica et Cosmochimica Acta*, **60**, 4231–4240.

Wolf, R.A., Farley, K.A. & Kass, D.M. 1998. Modeling of the temperature sensitivity of the apatite (U–Th)/He thermochronometer. *Chemical Geology*, **148**, 105–114.

Zahno, C., Akçar, N., Yavuz, V., Kubik, P.W. & Schlüchter, C. 2009. Surface exposure dating of Late Pleistocene glaciations at the Dedegöl Mountains (Lake Beyşehir, SW Turkey). *Journal of Quaternary Science*, **24**, 1016–1028.

Zaun, P.E. & Wagner, G.A. 1985. Fission-track stability in zircons under geological conditions. *Nuclear Tracks*, **10**, 303–307.

Zeitler, P.K., Herczig, A.L., McDougall, I. & Honda, M. 1987. (U–Th)/He dating of apatite: A potential thermochronometer. *Geochimica et Cosmochimica Acta*, **51**, 2865–2868.

Received 26 November 2012; revised typescript accepted 2 April 2013.
Scientific editing by Philip Hughes.